scientific reports

Check for updates

OPEN

Assessment of building damage from the 2020 Sivrice earthquake using a satellite based rapid seismic screening method

Yusuf Gedik[1], Orkan Özcan[1], Mihrimah Özmen[2]✉, Okan Özcan[3] & Semih Sami Akay[4]

Apart from inducing extensive damage rapidly across vast areas, earthquakes also have enduring consequences as they elevate stress levels in the neighboring regions where seismic activity persists. Although later destructive earthquakes, such as the February 6, 2023 Kahramanmaraş events, further highlighted the seismic vulnerability of the region, this study specifically focuses on assessing the impacts of the January 24, 2020 Sivrice Earthquake (Mw 6.7) on residential areas. After expert assessments of post-earthquake building damage, geolocated and damage-classified buildings were further analyzed through optical and Synthetic Aperture Radar (SAR) satellite imagery. Land classification was performed using optical images and a comparison was made between land class changes and building coordinates to detect collapsed buildings. Collapsed buildings were identified with 89.1% accuracy by analyzing land-use class changes from settlement to bare land between pre- and post-earthquake SVM-based classifications of optical images. Advanced Interferometric Synthetic Aperture Radar (InSAR) techniques, specifically Persistent Scatterer (PS) and Small Baseline Subset (SBAS) methods, were employed using SAR satellite imagery to calculate buildings' annual surface velocities for pre-earthquake dates. Correlation analyses were performed to assess the relationship between building damage classes and the key parameters of epicentral distance of the building, fault distance, the Earthquake Design Class (EDC), geological formation (i.e., Vs30), building type (RC or masonry), number of storeys, surface velocity, and Coulomb stress in order to predict building damage from possible earthquakes in advance by using pre-earthquake data and remote sensing (RS) methods. The damage estimation map was generated by integrating RS and geographic information system (GIS) methodologies, which included results of the correlation analysis that highlighted the dominance of the fault distance of the building, number of storeys, EDC, and surface velocity influencing damage severity. Thus, for seismic risk prioritization of buildings, RS and GIS-based first-stage assessment methods can be deployed as a rapid alternative to Rapid Visual Screening (RVS) methods since the need for one-by-one data collection from buildings by site survey is no longer necessary.

Earthquakes, among the most catastrophic natural disasters, wield a profound impact on extensive areas, causing harm to settlements and, consequently, human lives. These seismic events substantially disrupt social life, particularly in residential areas near their epicenters. Turkey, situated on significant faults, including the North Anatolian Fault Zone (NAFZ) and East Anatolian Fault Zone (EAFZ), is especially susceptible to seismic activity. Furthermore, the triple junction regions intersecting with the Ölüdeniz Fault position Turkey among the nations most significantly impacted by earthquakes[1].

Nowadays, research investigations into the destructive impacts of earthquakes are gaining heightened significance. Notably, the surge in the deployment of earth observation satellites has expedited the detection of earthquake-induced damage, facilitating field studies to be accomplished in significantly shorter durations.

In the realm of RS technologies, optical images are commonly employed to scrutinize alterations in land use, while SAR images frequently find application in investigating ground movements during field studies. The

[1]Eurasia Institute of Earth Sciences, Istanbul Technical University, Istanbul 34469, Turkey. [2]Industrial Engineering Department, Erciyes University, 38030 Kayseri, Turkey. [3]Department of Civil Engineering, Akdeniz University, 07070 Antalya, Turkey. [4]Department of Map and Cadastre, Istanbul Topkapi University, 34020 Istanbul, Turkey. ✉email: mihrimah@erciyes.edu.tr

popularity of satellite images in contemporary research is attributed to their capacity to operate on a large scale, conduct efficient and time-saving analyses, and attain a level of accuracy in line with results obtained through field studies.

Conducting damage assessment studies promptly after an earthquake is of paramount importance. Currently, these studies are swiftly executed through RS technologies and GIS methods. Aerial photographs captured during flights post-earthquake play a crucial role in detecting collapsed buildings. Various methods, including digital elevation model (DEM) generation from obliquely taken aerial photographs and building shadow analysis, contribute to the highly accurate identification of collapsed structures[2–4]. The automated detection of collapsed buildings is achievable using the Differential Interferometric Synthetic Aperture Radar (DInSAR) method. This method relies on radar images captured both before and after the earthquake, leveraging the low coherence observed in the interferogram for precise identification[5,6]. Moreover, employing multiple time-series SAR images along with the PSInSAR and SBAS methods allows for the precise identification of displacement events, including subsidence and uplift in specific areas, with millimeter precision. Additionally, this approach enables the extraction of ground surface velocities[7].

RS solutions, including optical satellite imagery and aerial photographs, are continuously used for building damage assessments. An automatic analysis method for detecting damaged buildings was introduced, utilizing regional structure and texture information extracted from post-earthquake IKONOS images and aerial photographs, primarily obtained after the Tangshan earthquake in 1976 but applied to the 2001 Bhuj earthquake. This method operates on the principle that intact buildings exhibit uniform texture characteristics, while damaged buildings are represented by lower grayscale values. Anomalies distinct from the surrounding area can be identified using a predefined threshold to distinguish between damaged and intact buildings[8]. Similarly, another study developed a damage detection system using aerial photographs and building vector maps to analyze the Gölcük earthquake, successfully differentiating between collapsed and intact buildings with producer accuracies of 81% and 94%, respectively[2]. Moreover, the damage level of each building can be identified through the analysis of roof shadows, where the ratio between the missing parts of the roofs and their corresponding shadow areas is used to determine the extent of the damage[9]. A further study employed a fusion of optical and radar satellite images to assess damages in residential areas related to the Izmit and Bam earthquakes, comparing the effectiveness of pixel-based and object-oriented processing methods for damage detection[10].

Damage assessment applications based on optical imagery are increasingly supported by SAR, DEM, Light Detection and Ranging (LiDAR) in order to achieve higher accuracy in the results. Brunner et al.[11] proposed a method for detecting building damage using QuickBird images captured before the earthquake and Terra-SAR-X images taken after the earthquake. In their method, the relevant parameters of the buildings were initially estimated from pre-earthquake optical images. The anticipated alteration traces in the SAR image post-earthquake were then estimated based on data obtained from both optical and SAR images. They calculated the similarity between the SAR image and the estimated image in the final processing step. Less similar areas were presumed to represent collapsed buildings. When applied to detect buildings affected by the damage caused by earthquakes, their method achieved an overall accuracy of approximately 90%.

NAFZ is one of the most seismically active regions in Turkey, and the Koyulhisar district of Sivas province, located within this zone, is notably affected by landslides and related ground displacements. In this context, horizontal displacements and landslide movements in the region have been identified using ASTER satellite imagery and DEM data through the application of the Co-Registration of Optically Sensed Images and Correlation (COSI-Corr) method, developed by the California Institute of Technology[12]. In Koyulhisar, horizontal displacements ranging from 1.0 to 8.6 m per year have been detected, demonstrating the potential applicability of this method for landslide analysis[13]. In the immediate aftermath of disasters, innovative methods that integrate SAR and LiDAR data have been increasingly employed to rapidly assess earthquake-induced damage. While SAR data are primarily used for large-scale ground displacement analysis following seismic events, LiDAR data enable building-scale change detection for evaluating damage within urban areas. The combined use of these two datasets has demonstrated the potential to enhance disaster preparedness by supporting effective damage assessment and first-response planning in post-earthquake scenarios[14].

Recent studies have sought to understand the mechanics of stress transfer better and rupture behavior along the EAFZ, particularly in the context of the 2020 Sivrice (Elazığ) earthquake. One such study investigated Coulomb stress changes before and after the mainshock using data from approximately 90 earthquakes ($M \geq 4.5$) with depths ranging between 7.5 and 30 km, recorded over the past 23 years within the EAFZ. Coulomb stress maps generated from the mainshock and its aftershocks revealed that stress propagated in both northeast and southwest directions, leading to compressional stress accumulation. Notably, regions around the Palu–Lake Hazar and Çelikhan–Gölbaşı segments were identified as critical zones with high seismic potential[15].

In the Ragon et al. study[16], a complementary approach, geodetic data were used to model the subsurface fault slip distribution through an unregularized Bayesian sampling method that incorporates physically plausible prior information and accounts for uncertainties in both the elastic structure and fault geometry. The results indicated that the Elazığ earthquake rupture was predominantly unilateral, featuring two disconnected slip regions likely shaped by structural complexity. Although some InSAR data collected up to one month after the mainshock may reflect postseismic deformation, observed surface displacements from one week to five months post-event did not exceed a few centimeters. The epicenter's precise location remains uncertain, with estimates placing it deeper than 16 km and showing up to 20 km variation between different institutional reports. While some models position the epicenter near the main fault bend, others suggest a location between bends, underscoring the significant influence of epicentral uncertainty on interpretations of rupture directivity. Despite these discrepancies, the rupture appears to have propagated unilaterally toward the southwest. Furthermore, the slip distribution pattern derived in this study diverges from models by Pousse-Beltran et al.[17], Cheloni and Akinci[18], which report peak slip values of 2 m. Instead, it shows greater consistency with the model proposed by

Melgar et al.[19], particularly in terms of the maximum slip location and rupture configuration. These similarities emphasize the necessity of incorporating a layered crustal model to achieve accurate slip estimations in the region. The 2020 Sivrice earthquake, which ruptured the Pütürge segment of the EAFZ, has been the subject of detailed investigations aiming to understand the rupture dynamics and structural characteristics of the region. A comprehensive study analyzed foreshocks occurring on 4 April and 27 December 2019, along with the mainshock that nucleated near a 10° bend in the fault trace. By integrating InSAR observations, seismological data, and fault modeling, the rupture was shown to have propagated west-southwest at approximately 2 km/s along a relatively simple fault structure before halting in the Lake Hazar basin—an established segment boundary within the EAFZ. The study identified a shallow slip deficit only partially compensated by afterslip, a notably slow rupture velocity, and substantial off-fault seismicity. These findings challenge simplified models of fault segmentation in the central EAFZ, suggesting that the 2020 event did not follow typical characteristic rupture behavior. The results further highlight the immature structural development of the fault and underline the importance of considering off-fault deformation in future paleoseismological and morphotectonic studies[17].

To investigate the impact of non-seismic factors on building damage, the types of structural damage caused by the Mw 6.7 Sivrice earthquake were examined. Analysis of concrete quality revealed that poor construction practices, such as lack of engineering services, substandard construction techniques, and low-quality materials, significantly contributed to structural damage. Existing buildings were found to be insufficiently earthquake-resistant, and many collapsed or severely damaged structures were not constructed in accordance with earthquake regulations. Beyond ground conditions, attention should be paid to appropriate material quality, construction supervision, and seismic design principles in regions with high seismic activity. Furthermore, it has been recommended that existing structures be analyzed and strengthened to withstand future earthquakes, and that building design irregularities, such as short columns and torsional irregularities, be minimized[20,21].

With future advancements in technology, rapid solutions for damage assessment will be provided through semi-automatic and automated analyses. Current studies, however, demonstrate semi-automatic solutions using SAR imagery and machine learning methods. By integrating high-resolution SAR data with building inventory information and ground shaking intensity maps, the study classifies building damage into multiple categories. Applying binary and multi-class classification models to four recent earthquakes, utilizing Damage Proxy Maps (DPMs) and ShakeMaps generated by the ARIA project, the study found that in certain cases, binary classification identified more than 50% of damaged buildings. The study demonstrated that for a holistic approach and higher accuracy, additional building characteristics, such as building construction type and structural integrity, should be integrated into the models[6].

Hacilar et al.[22] utilized the official earthquake damage dataset provided by the Ministry of Environment, Urbanization, and Climate Change (MoEUCC) to develop a cost-sensitive parallel Artificial Bee Colony–Artificial Neural Network (ABC–ANN) model for multi-class earthquake damage classification. By incorporating a misclassification cost matrix and applying GPU/CPU parallelization with vectorization, the study achieved improved classification accuracy and reduced computational time compared to conventional methods. Their results highlight the value of advanced computational approaches in enhancing post-earthquake damage assessment and supporting disaster management strategies.

In this study, we move beyond simply identifying land-use changes in earthquake-damaged buildings using optical image classification. Our approach focuses on systematically examining buildings that experienced severe damage during the earthquake to gain a better understanding of the underlying factors influencing their vulnerability. A multi-source RS strategy was implemented to investigate building damage patterns, combining land use classification from multi-temporal Sentinel-2 optical imagery (10 m resolution) with advanced InSAR time-series techniques (PSInSAR and SBAS) applied to Sentinel-1 SAR data to calculate ground deformation velocities.

Annual surface velocity rate maps were generated and correlated with building damage grades to evaluate the influence of ground motion on structural vulnerability. By linking deformation rates to buildings with known damage levels, a comprehensive geospatial dataset was constructed, including annual surface velocities, Coulomb stress changes, geological formations, Vs30 shear-wave velocity distributions, building typologies, number of storeys, and proximity to active fault segments. Through integrated spatial analysis, key parameters contributing to increased seismic vulnerability and building damage were systematically examined, and a predictive seismic damage map was produced.

Study area and dataset

The study area given in Fig. 1 encompasses the city center of Elazığ with the fault, epicenter and building locations for the 6.7 Mw left-lateral strike-slip earthquake on 24 January 2020. Additionally, the spatial relationships between the fault, the epicenter, and the buildings are visually represented in Fig. 1. The geological map of the study area, crafted by the Mineral Research and Exploration General Directorate (MTA)[23], was incorporated to ascertain the geological formations corresponding to the building coordinates in which the epicentral location was marked as well (Fig. 1).

Figure 2 depicts the USGS-generated ShakeMap for Turkey's January 2020 Mw 6.7 Sivrice earthquake which is integral to the earthquake damage assessment process, as it delineates the geographic extent of the area potentially impacted by seismic activity and serves as a critical input in RS analyses used to predict damage outcomes. Peak Ground Acceleration (PGA), typically determined from strong motion records or estimated using ground motion prediction equations based on earthquake source parameters, site conditions, and path effects[25], is presented in Fig. 3 as the spatial distribution of projected ground motion parameters across the study area[26].

Figure 4 shows the Coulomb stress map of the Sivrice obtained from the events before the Earthquake[15]. The average shear wave velocity in the uppermost 30 m of the soil (Vs30) was obtained from Heath et al.[27], and the

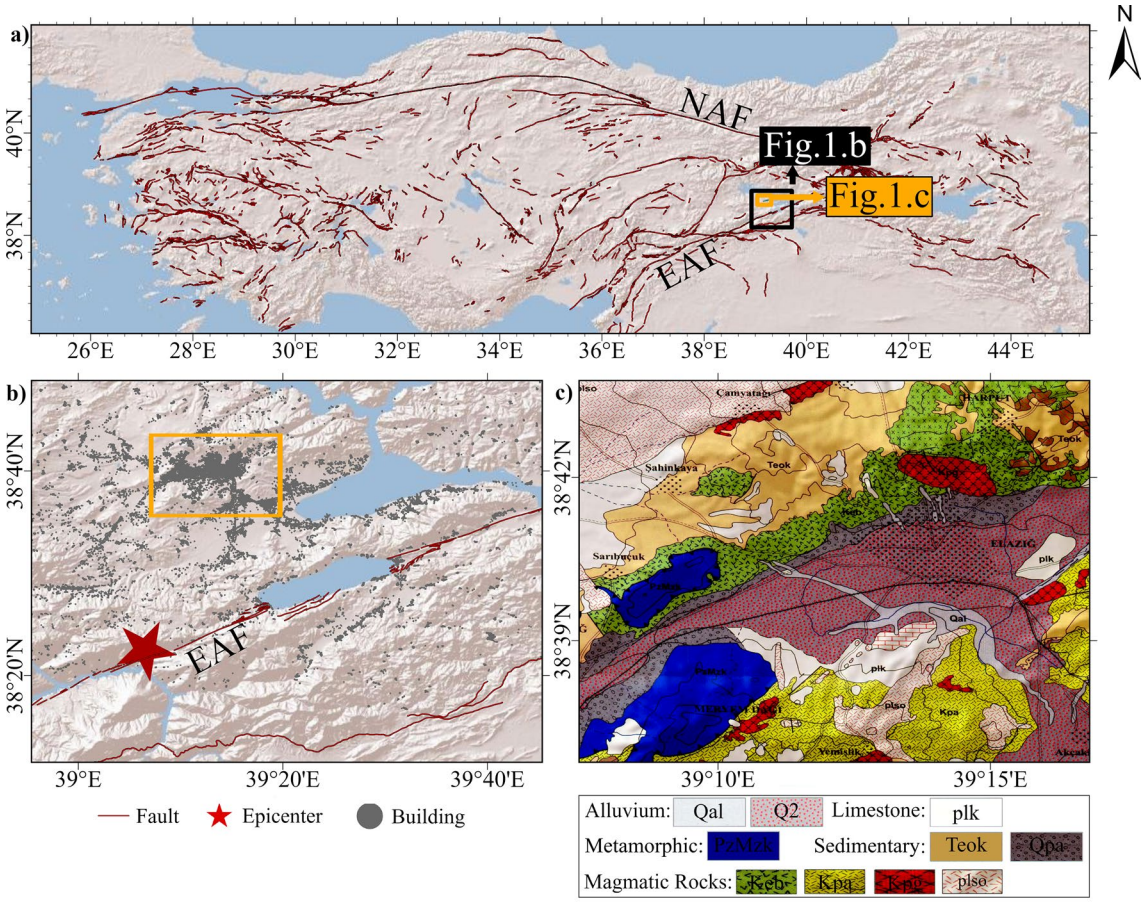


Fig. 1. Overview of the study area: (**a**) Geographical location of the study area (NAF: North Anatolian Fault, EAF: East Anatolian Fault), (**b**) Display of the earthquake epicenter, fault lines, and building coordinates, (**c**) Geological map corresponding to the area covering the building coordinates obtained from the MTA[23]. The spatial grid reference shown in panel (**b**) applies to the extents of Figs. 2, 3, 4, 5 and 12, 13, while the grid reference in panel (**c**) applies to the extents of Figs. 6, 16, 17, 18, 19, and 23. The maps were generated using ArcGIS Pro[24].

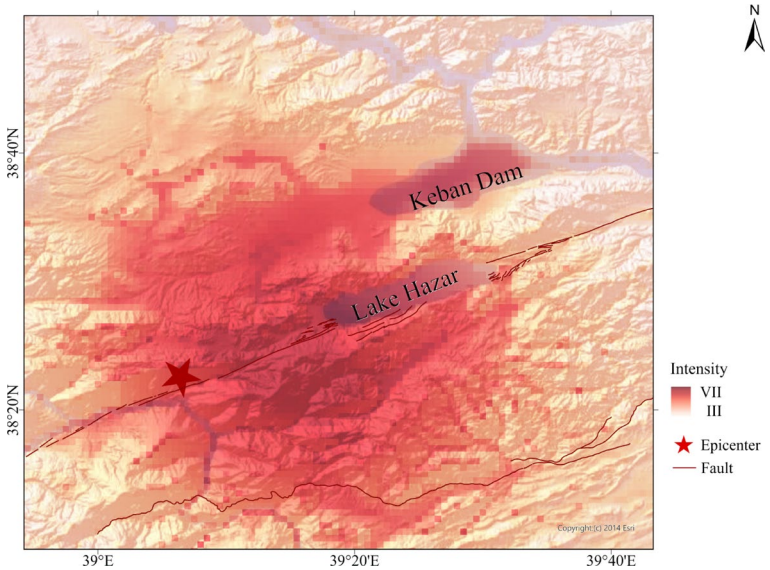


Fig. 2. Macroseismic Intensity Map of the Sivrice Earthquake[26]. The map was generated using ArcGIS Pro[24].

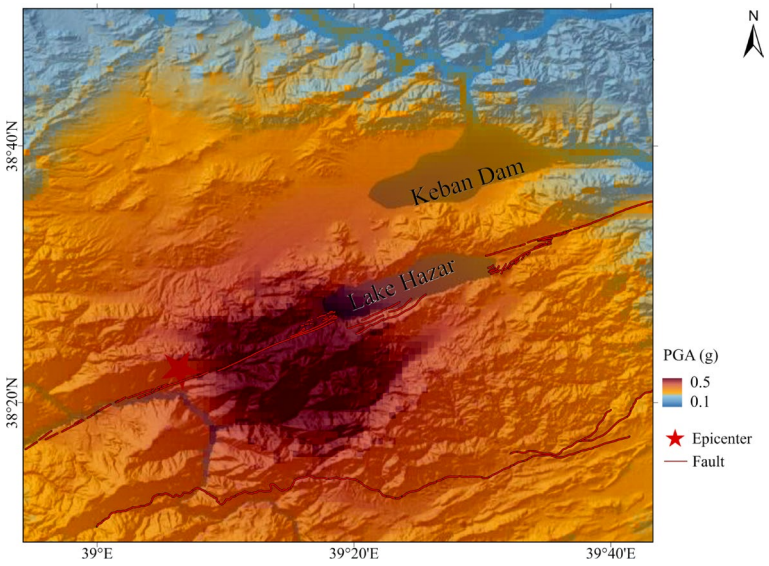


Fig. 3. Peak Ground Accelerations of the Sivrice Earthquake[26]. The map was generated using ArcGIS Pro[24].

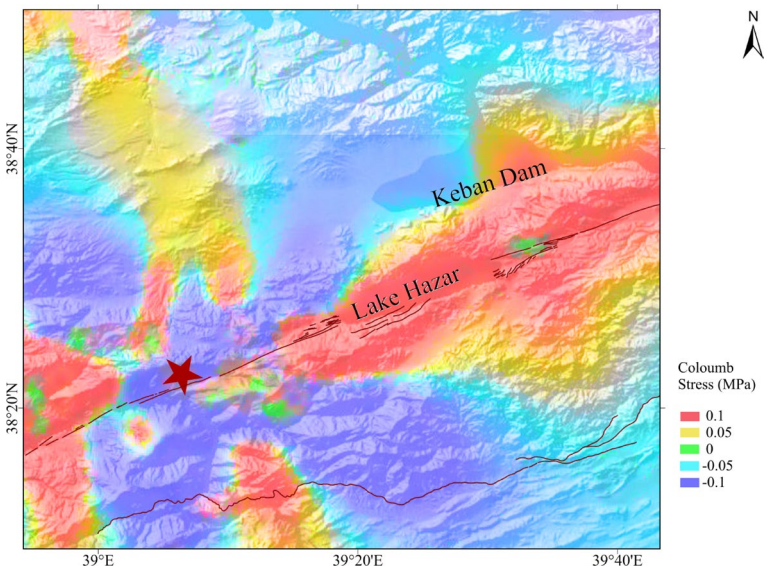


Fig. 4. Coulomb Stress distribution prior to the Sivrice Earthquake, modified from Alkan et al.[15].

Vs30 Map of Elazığ City Center was generated based on this dataset as shown in Fig. 5. Figure 6 illustrates the data digitized from the MoEUCC, with the number of storeys of the buildings in the study area.

Building damage assessments conducted by authorized personnel from the MoEUCC are rooted in observational examinations, which involve identifying building types and damages in both load-bearing elements (e.g., columns, shear walls, beams) and non-bearing elements (e.g., partition walls, cladding) of buildings. Upon MoEUCC inspections, the buildings are categorized into damage classes ranging from non-damaged (Grade 1), slightly damaged (Grade 2), heavily damaged (Grade 3), severely damaged (Grade 4), collapsed (Grade 5), and obtained data in field studies were transferred to the GIS environment[28].

The first source of satellite imagery utilized in this study comprises optical images. As part of the investigation, a total of 8 Sentinel-2 optical satellite images from various months were employed to identify buildings that collapsed during the earthquake. To enhance the precision of earthquake impact assessment, images were acquired and scrutinized for several months following the earthquake to ascertain the demolition date of structures experiencing substantial to heavy damage and severe damage. Based on the outcomes of this analysis, the satellite images for subsequent analyses were determined.

In the study area, buildings classified under the 4th-degree damage category were almost demolished in a controlled manner by authorized professionals within six months following the earthquake. Accordingly, for optical imagery, the selected post-earthquake dates were determined considering the completion of the

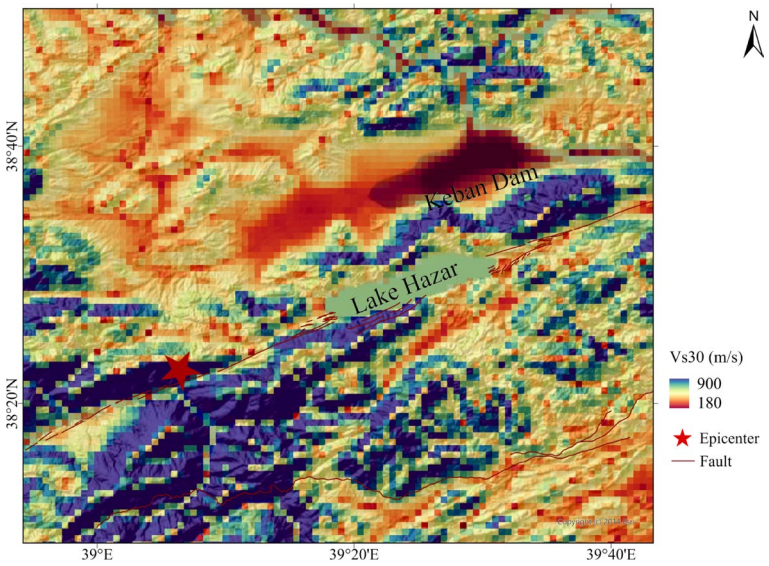


Fig. 5. Shear Wave Velocity (Vs30) Map of Elazığ City Center, generated using the hybrid Vs30 dataset provided by Heath et al.[27] and processed in ArcGIS Pro[24].

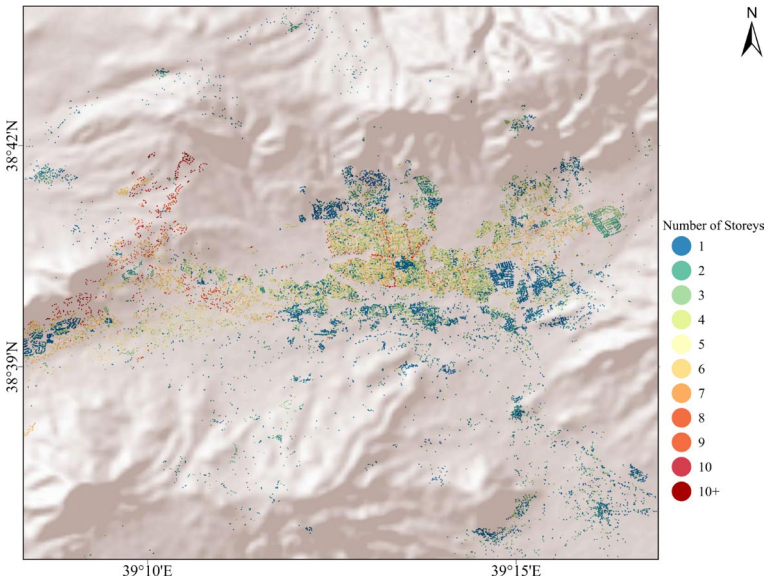


Fig. 6. Number of storeys in the study area. The map was generated using ArcGIS Pro[24].

controlled demolition process. In the SAR segment of the study, a comprehensive analysis was conducted to determine the annual ground velocities by utilizing the DInSAR, PSInSAR, and SBAS methods. 243 Sentinel-1A and 1B Single Look Complex (SLC) SAR images, acquired in the ascending and descending orbit, were employed for this purpose which covered the five years (2015–2020) preceding the earthquake[29].

Method

The study further scrutinized the influence of various parameters on the damage class of the buildings by integrating the results from both optical and SAR images with the fieldwork data using the flowchart given in Fig. 7. We applied supervised classification to Sentinel-2 satellite imagery with a spatial resolution of 10 m, acquired before and after the earthquake, to determine land use classes. We then compared land use changes between the two dates with building damage coordinates to identify collapsed buildings through optical satellite data. We used two different Sentinel-1 SAR images to determine surface displacements caused by the earthquake using the DInSAR technique. Furthermore, we produced annual surface velocity rate maps of the study area by applying advanced InSAR techniques (PS and SBAS) to five years of pre-earthquake Sentinel-1 SAR imagery. Finally, we integrated the surface velocity data with various geospatial layers such as Vs30, Coulomb stress, fault

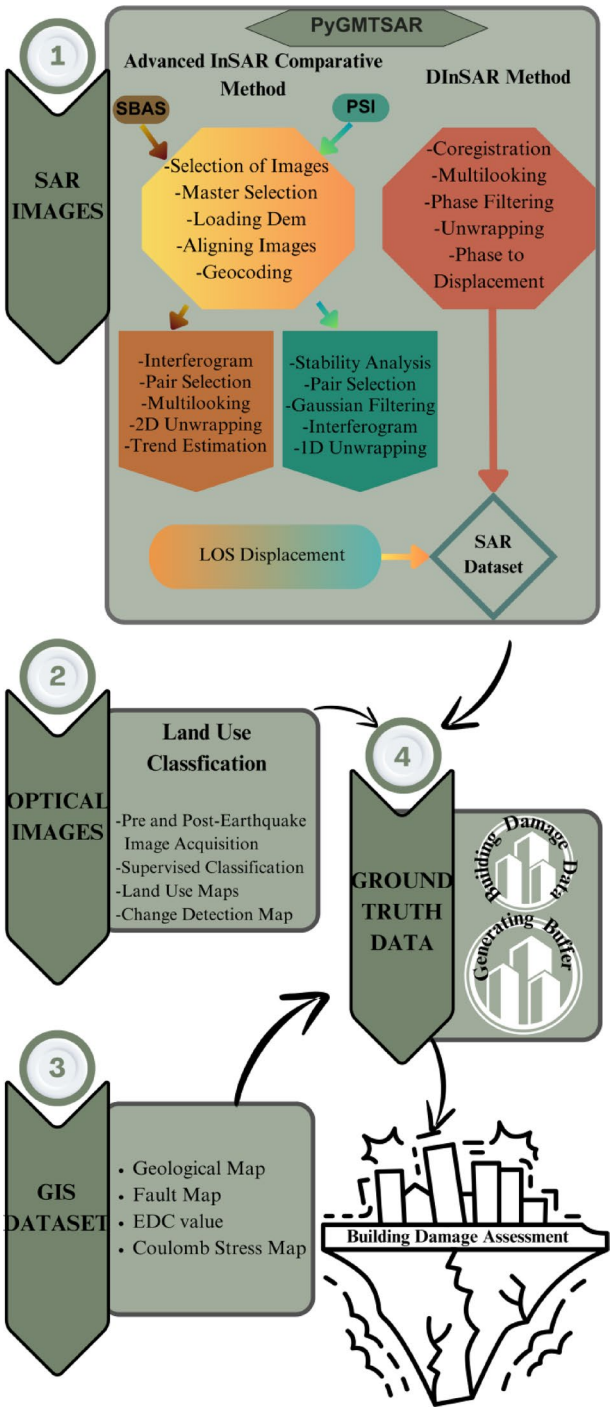


Fig. 7. Flowchart of the building damage assessment.

maps, geological maps, building types, and building height coefficients to analyze the parameters influencing building damage.

Land use classification

We used optical satellite images to identify changes in the settlement areas within the study region. For the pre-earthquake images, months with low cloud cover near the earthquake date were chosen as far as possible, while months witnessing the demolition of heavily damaged and urgently demolishable buildings were preferred for the post-earthquake images. Further, the acquired building inventory data from MoEUCC, which comprises the building type, damage classes, and the list of dates when all severely damaged buildings were demolished, was digitized for comparison of the analysis results based on the post-earthquake optical images. To account for potential misalignments between point coordinates from fieldwork and buildings on the map, as well as

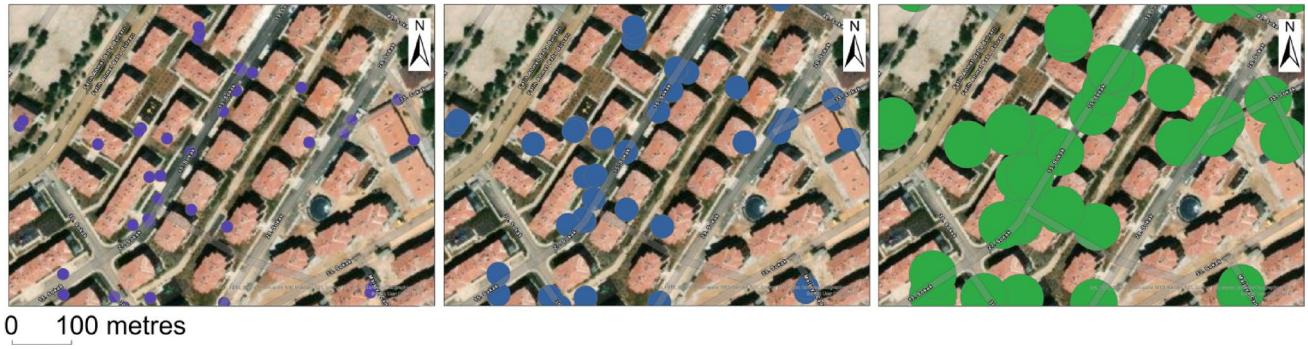


Fig. 8. Demonstration of 5, 10 and 15 m buffer applications on World Imagery basemap (purple: 5, blue: 10, green: 15 m)[30].

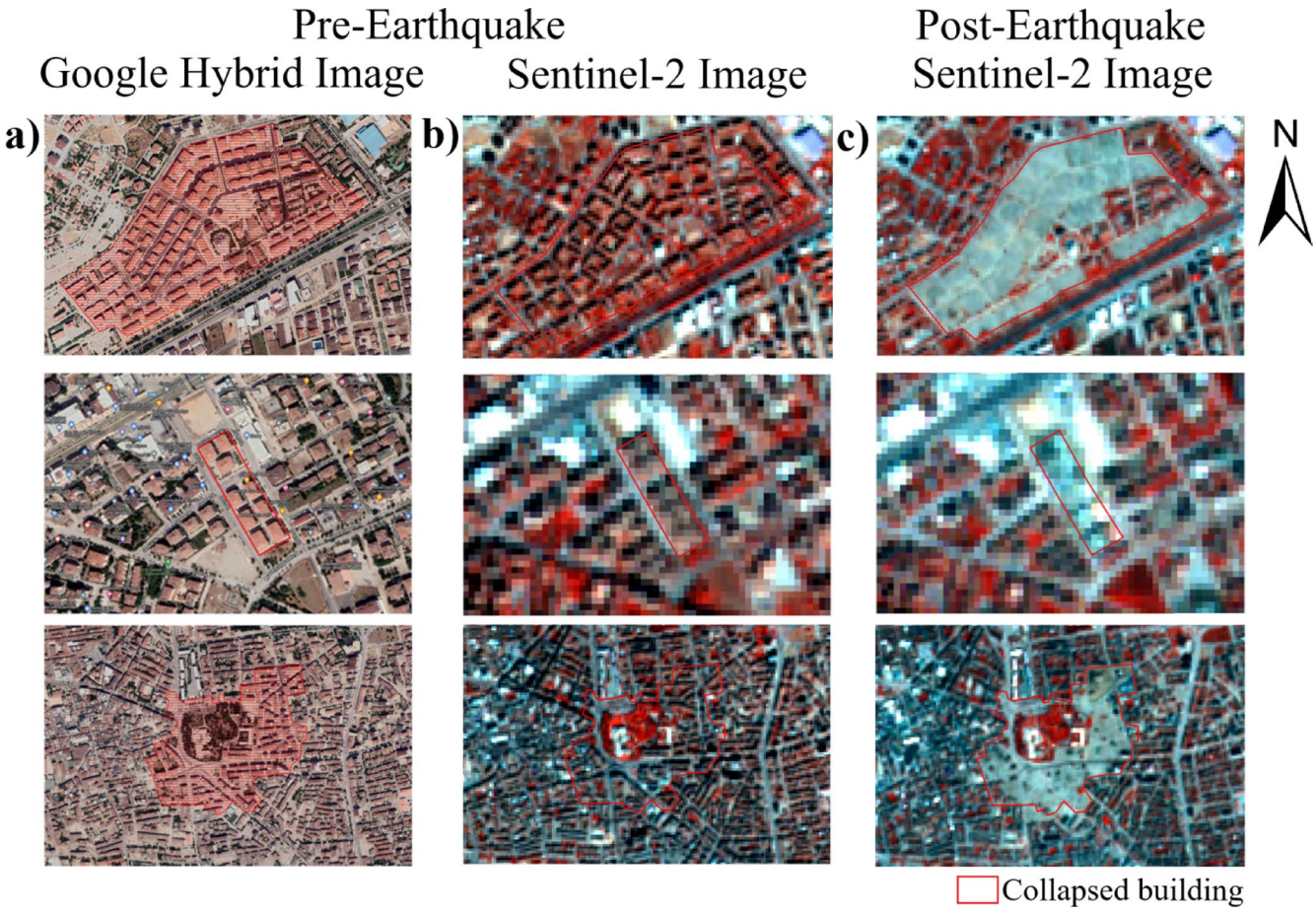


Fig. 9. (**a**) Collapsed buildings in the study area, marked on the Google Maps Hybrid View, (**b**) pre-earthquake view, and (**c**) post-earthquake view using a false-color band combination of Sentinel-2 optical images[31], where damaged or bare surfaces appear in blue or light tones, while red tones indicate vegetation such as trees and other plants. The figure was prepared using ArcGIS Pro[24,30].

differences in data resolutions, a buffer operation was systematically conducted with diameters of 5, 10, and 15 m on the point coordinates. This iterative process aimed to determine the most appropriate diameter values to encompass the buildings, and the visual representation of this buffer analysis is provided in Fig. 8. The obtained damage classes were compared with the damage classes given in the building inventory data to observe the coherence. These identified areas were subsequently cross-referenced with building damage data obtained through fieldwork. Figure 9 depicts pre- and post-earthquake satellite images utilizing false-color combinations for the three neighborhoods in Elazığ city center that experienced the most significant damage from the earthquake (Neighborhoods of Abdullah Paşa, Mustafa Paşa, and Sürsürü).

Since building demolition and reconstruction vary over time, we couldn't assign a single, definitive accuracy value for change detection based on multiple temporal images. Change detection using only two images often failed to capture these temporal dynamics accurately. In many cases, buildings appeared collapsed in early images but showed signs of reconstruction in later ones. Consequently, classification models tended to label these areas as built-up again. By utilizing numerous images from different dates, we conducted a time-series analysis on the optical data. We examined changes in land use classes within buffer zones around building coordinates across these temporal intervals. Once a buffered building coordinate area changed from a residential class to a different land use class for the first time, we considered that the building demolition had occurred. In subsequent analyses, we checked whether the new non-residential land use classification persisted over later dates. This approach enabled us to dynamically monitor building demolition events based on temporal changes in land use detected from the imagery. Supervised classification methods (SVM, ML, and KNN) were applied to images categorized into pre- and post-earthquake periods to generate Land Use and Land Cover (LULC) maps (Fig. 10). Herein, bands 2, 3, 4, and 8 of Sentinel-2 optical satellite images, with a resolution of 10 m, were selected for the analysis using false-color images. For the SVM-based classification, the ArcGIS Pro supervised classification tool was used. In this implementation, hyperparameters—including kernel type, gamma, and penalty values—are internally optimized by the software and were not explicitly specified by the user. Training and validation were performed using manually selected samples for each land-cover class, and classification accuracy was assessed through confusion matrices generated within ArcGIS Pro.

Support Vector Machine (SVM), Maximum Likelihood (ML), and K Nearest Neighbor (KNN) classifiers were applied to generate high-accuracy LULC maps, enabling the detection of built-up areas and the assessment of structural changes caused by the earthquake. Accuracy was evaluated using 300 control points (see Supplementary Fig. S1, Table S3, and Table S4), high-resolution reference maps, and confusion matrices, with SVM showing the highest performance; it was therefore used for subsequent time-series analyses to detect collapsed or demolished buildings (Table 1). The Kappa coefficient[32] was employed to quantify agreement between classification results and reference data.

The Otsu thresholding method was applied to extract built-up areas from optical imagery efficiently. Unlike multi-class supervised techniques, Otsu focuses on binary segmentation based on pixel intensity, reducing

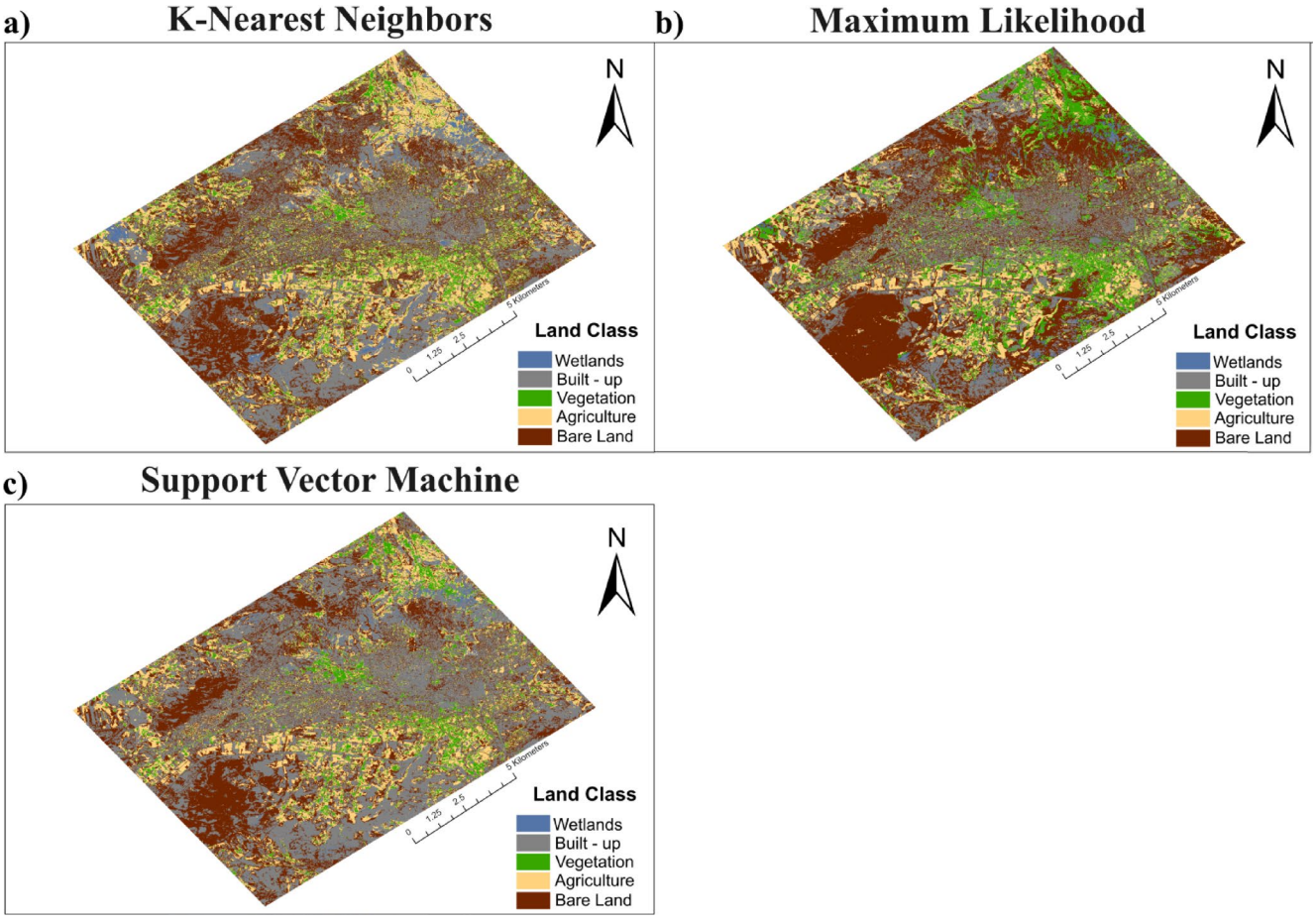


Fig. 10. Land use/land cover (LULC) map of the study area, generated by the authors using ArcGIS Pro 3.2. The legend categories include wetlands (areas dominated by water-saturated soils), built-up areas (urban and developed regions), vegetation (natural plant cover), agriculture (cultivated lands used for farming), and bareland (exposed soil or rock with minimal vegetation. The figure was prepared using ArcGIS Pro[24].

Method	SVM		KNN		ML	
	Pre	Post	Pre	Post	Pre	Post
% Accuracy	90.33	91.00	81.33	85.67	83.00	81.67
Kappa	0.90	0.90	0.81	0.86	0.83	0.82

Table 1. Land use classification results.

the need for training datasets and class-specific parameters. This streamlined approach is particularly useful for rapid post-disaster assessments[33–35]. While the method may not capture intra-class spectral variability or contextual information as accurately as advanced supervised algorithms, its simplicity and speed make it suitable for preliminary or large-scale urban mapping efforts. In our study, we applied the Otsu method to threshold the binary Built-Up Index (BUI) image, and validated the extracted built-up areas by comparing them with 300 selected control points across the study region, ensuring a reliable assessment of classification accuracy (see Supplementary Table S5 online). This unsupervised and reproducible nature of the method allows for faster deployment in emergency response scenarios, where timely insights are critical[36].

DInSAR method

We employed the DInSAR method to determine post-earthquake displacements by generating interferograms from pre- and post-earthquake images. Following the creation of an interferogram with two SAR images, the DInSAR process advances through phase unwrapping. The subsequent steps involve converting the phase into displacement values, ultimately producing displacement maps. The phase difference serves as a crucial parameter for computing the Line of Sight (LOS) displacement. Any movement or deformation along the LOS induces a phase change in the radar signal, providing a measure of ground displacement[37]. The result of InSAR processing is commonly represented as a LOS displacement map. Each pixel in the image reflects the extent of displacement along the radar LOS. As the ground moves away from the satellite, the values increase positively, and as the ground gets closer to the satellite, the values increase negatively[38].

Advanced InSAR method

To assess post-earthquake building displacements and their correlation with pre-earthquake surface velocities, we applied PSInSAR and SBAS methods to 283 Sentinel-1A and 1B SAR images acquired over both ascending and descending orbits (see Supplementary Table S1 online). Images spanning five years prior to the earthquake were processed using the PyGMTSAR package[39,40] to derive high-precision surface velocity maps. PSInSAR focuses on identifying stable features on the Earth's surface, such as buildings or rock formations, which serve as reference points for monitoring relative motion over time. SBAS, in contrast, emphasizes multi-temporal interferogram analysis to capture subtle surface variations. Both methods share a common processing framework, including pre-processing, interferogram generation, phase unwrapping, atmospheric correction, time-series analysis, inversion for deformation estimation, and displacement map generation. The PS method additionally includes stability analysis, pair selection, and Gaussian filtering, whereas SBAS directly proceeds to phase unwrapping. This integrated workflow enabled robust detection and quantification of surface deformations with high spatial and temporal resolution.

The analysis faced several practical challenges: the use of two different satellites, ascending and descending tracks, and the long temporal coverage considerably increased the number of interferograms and computational load. Seasonal snow cover and the presence of water bodies in the study area also required careful attention during coherence and atmospheric filtering steps to ensure accurate measurements. For SBAS processing, interferograms were multi-looked to a 15 m effective resolution, and a coherence-weighted least-squares solution was used to derive line-of-sight (LOS) displacements. Pixels with a mean coherence lower than 0.6 were masked from the inversion. To mitigate long-wavelength atmospheric delays, orbital ramps, and residual topographic effects, a regression-based trend correction was applied using topography, incidence angle, and low-order spatial polynomial terms. For PS analysis, persistent scatterers were selected based on temporal phase stability, and the SBAS-derived trend component was incorporated to suppress atmospheric and orbital artifacts. LOS displacements were estimated through a one-dimensional unwrapping and a coherence-weighted least-squares inversion, applying the same 0.60 coherence threshold for consistency.

The derived surface velocity maps were subsequently correlated with building damage grades to evaluate the influence of tectonic strain on structural vulnerability. In addition to surface velocity data, various GIS layers—including Coulomb stress changes, geological formations, Vs30 shear-wave velocity distributions, building typologies, number of storeys, and proximity to active faults—were integrated with the building inventory. This multi-parameter geospatial analysis enabled a detailed assessment of factors potentially influencing structural vulnerability, indicating that areas with higher surface velocity rates were generally associated with greater building damage. Figure 7 illustrates the overall processing workflow, highlighting the steps where methodological choices and study-specific adjustments were applied.

Results

This study focused on assessing the effects of earthquakes on residential areas by employing optical and SAR satellite images and integrating RS and GIS methods. The study aimed to scrutinize the concordance of the results with existing damage detection studies. Furthermore, an evaluation was conducted to identify the key

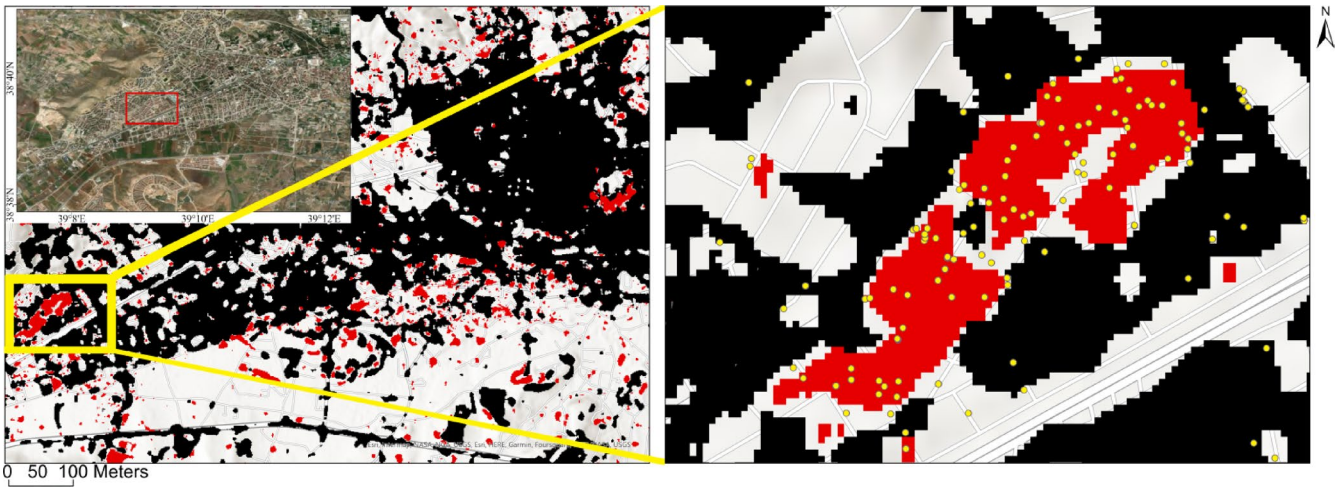


Fig. 11. Overlapping of the land class change map with building damage distribution (from severely damaged to collapsed buildings). The left panel shows the wider study area, with the yellow rectangle indicating the sub-area highlighted on the right. The right panel presents a zoomed-in view from a neighborhood where most buildings were destroyed. Yellow dots indicate the coordinates of severely damaged to collapsed buildings (damage grades 3–5) with a 5-m buffer applied; black areas represent settlement classes that have not changed, and red areas denote changes in settlement areas). The figure was prepared using ArcGIS Pro[24,30].

Damage class	Correctly classified (TP)	Fieldwork count	Recall (%)	Precision (%)	Kappa (%)
BUFFER 5 m					
Grade 4	554	616	89.9	85.2	0.781
Grade 5	248	267	92.9		
BUFFER 10 m					
Grade 4	518	616	84.1	80.6	0.662
Grade 5	240	267	89.9		
BUFFER 15 m					
Grade 4	472	616	76.6	71.1	0.499
Grade 5	225	267	84.3		

Table 2. Comparison of classification results and field studies in Elazığ city center.

parameters contributing to earthquake-induced damage. This involved analyzing surface velocity rates alongside active fault maps, geological maps, and building inventory in a comprehensive manner.

Optical image analysis results

The SVM method was utilized to generate LULC maps, enabling the analysis of alterations in residential areas pre- and post-earthquake through change detection. Residential areas that remained unchanged after the earthquake were depicted in black, whereas those undergoing changes were marked in red (Fig. 11). The analysis involved examining the coordinates associated with damage classes and overlaying them on the land use change map to identify potential correlations.

In Elazığ city center, a comparison between the buildings examined during field studies and the land class map derived from optical image classification revealed that, with a 92.9% accuracy rate, the land class of 248 out of 267 collapsed buildings (Grade 5) transitioned from residential to a different land class. Additionally, for the 554 out of 616 buildings marked as Grade 4 in the field studies, located on grounds classified as settlements before the earthquake, the land class changed after the earthquake, achieving an 89.9% accuracy rate through satellite image classification. Table 2 presents the accuracy percentages based on satellite imagery and field data for each damage class.

SAR image analysis results

DInSAR

The DInSAR method was applied to the pre- and post-earthquake SAR SLC satellite images which were selected as close as possible to the date of the earthquake to avoid noise due to atmospheric condition variations. As such, the maximum ground displacements due to subsidence and uplift were determined on images obtained from the ascending and descending orbits of two satellites, Sentinel-1A and Sentinel-1B. As a result of the DInSAR analysis, the horizontal displacement results are presented in Fig. 12, while the vertical displacement results are

illustrated in Fig. 13. Additionally, the results indicate that the maximum calculated subsidence values range between 173 and 293 mm, while the uplift values range between 202 and 255 mm, as shown in Table 3. The results appear to be consistent with the findings of Konca et al.[41].

Advanced InSAR (PS and SBAS)

The impact of surface velocity on damage severity was analyzed using the data presented in Table 4. Interferograms were generated using satellite images from the past five years to estimate surface velocities. The baseline distances were computed, and only those with a baseline distance of less than 150 m were included in the analysis (Fig. 14). Surface velocities were derived using the PS and SBAS methods, which are advanced InSAR techniques. A comparative analysis of the results demonstrated that both methods produced similar outcomes in urban areas (Fig. 15). Finally, annual surface velocity maps obtained from InSAR time-series analysis were generated for the study area, and Fig. 16 demonstrates the quantified building inventory to assess the correlation between surface velocity and building damage classes.

Results of RS and GIS integration

To estimate earthquake-induced damage based on pre-event data, surface velocity maps covering the past five years were derived and combined with critical datasets, including the geological map with Vs30, Coulomb stress distribution, building inventory, and detailed typological information (see Supplementary Table S6). Table 5 summarizes observed damage patterns across different geological formations. Damaged building coordinates were imported into a GIS environment, allowing extraction of relevant parameters from raster datasets, such as building type, number of storeys, surface velocity, geological formation, Coulomb stress, distance to faults, Vs30, and EDC values.

Each parameter was assigned a value based on whether it contributed positively or negatively to the building's structural resistance. The cumulative score of all parameters for each coordinate was used to assign a numerical resilience index to every building. Based on this index, we classified the top 5% of values as Grade 5 and marked these buildings on the map accordingly. The following 5% (i.e., the 5–10% range) was categorized as Grade 4, while values within the 10–20% range were designated as Grade 3. We then compared these results with field survey data, where buildings were independently labeled according to observed damage levels. Figure 17 illustrates the damage classification of buildings along with the spatial distribution of the corresponding damage levels, ranging from non-damaged (Grade 1), slightly damaged (Grade 2), heavily damaged (Grade 3), severely

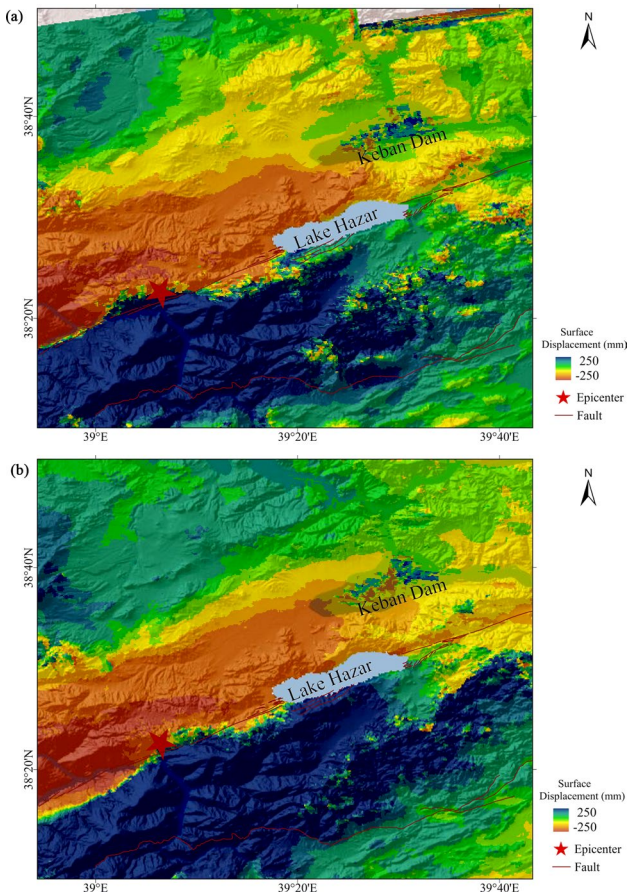


Fig. 12. Horizontal (**a**, **b**) displacement results of the DInSAR method (Top: ascending, Bottom: descending orbit). The maps were generated using ArcGIS Pro[24].

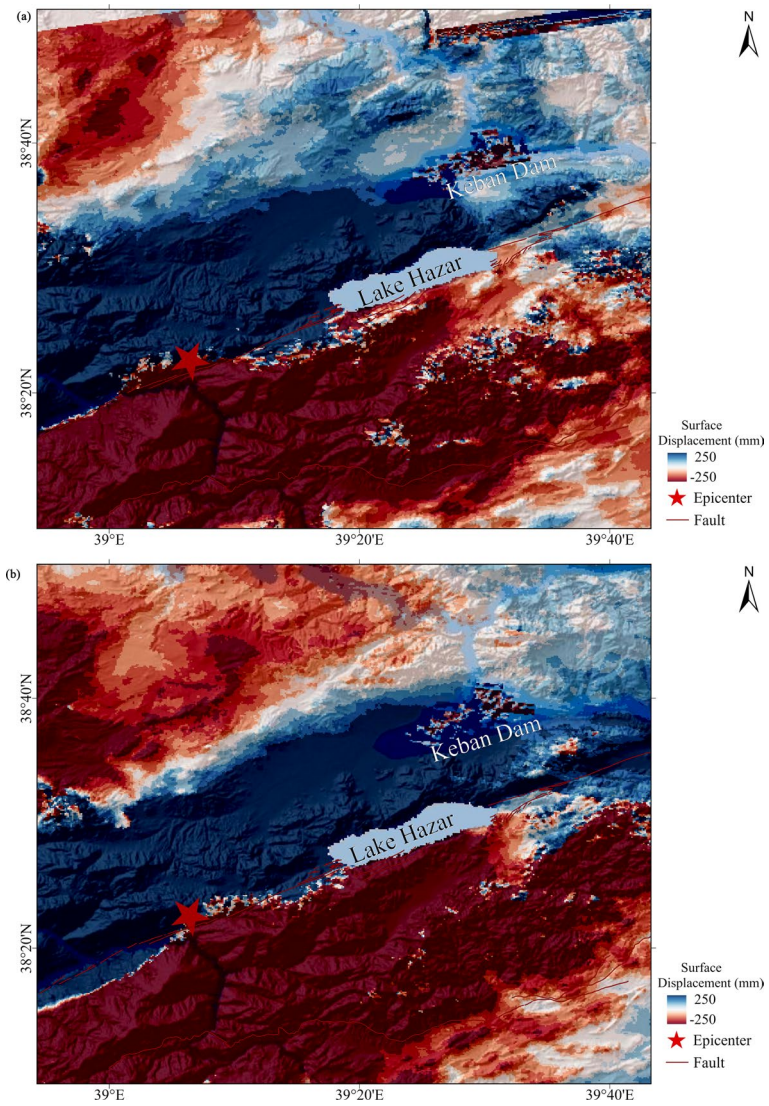


Fig. 13. Vertical (**a**, **b**) displacement results of the DInSAR method (Top: ascending, Bottom: descending orbit). The maps were generated using ArcGIS Pro[24].

Ground displacement values (DInSAR)		
	Maximum values (mm)	
Satellite	Subsidence	Uplift
S1A Ascending	173	254
S1A Descending	248	202
S1B Ascending	222	255
S1B Descending	293	211

Table 3. DInSAR results.

damaged (Grade 4), to collapsed (Grade 5). Figure 18 shows the map of collapsed buildings determined by the classification method of optical images. Figure 19 presents buildings classified as having third-, fourth-, and fifth-degree damage in the digitized building inventory.

To determine the primary factors contributing to building damage, we carried out a comprehensive multi-parameter analysis integrating diverse datasets. We categorized ground formations—critical to structural resilience—along a continuum from loose alluvial soils to more compact, stable substrates, reflecting increasing load-bearing capacity. Surface velocity, a key proxy for soil stiffness and seismic wave amplification, was similarly

Orbit	Ascending		Descending		
Method	PS	SBAS	PS	SBAS	Average (mm/yr)
Grade 1	2.6	2.9	2.2	2.1	2.5
Grade 2	2.6	1.0	2.4	1.1	1.8
Grade 3	3.4	1.4	3.1	1.2	2.3
Grade 4	3.9	2.2	3.5	2.4	3.0
Grade 5	4.5	3.5	4.6	3.0	3.9

Table 4. PS and SBAS average velocity results.

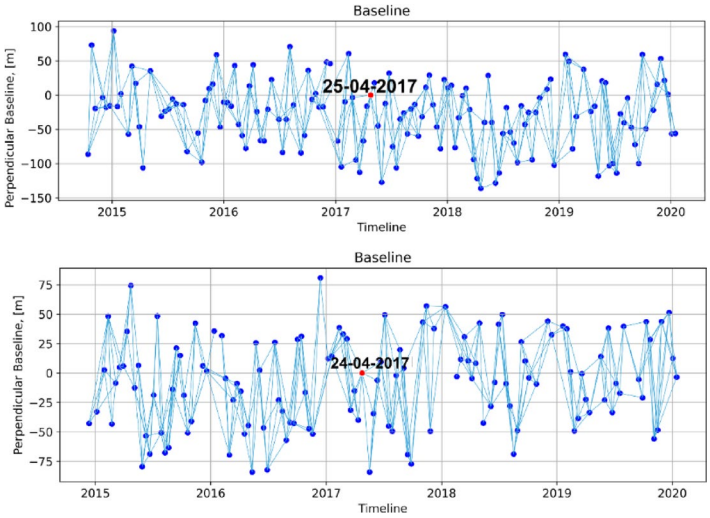


Fig. 14. SBAS Baseline analysis (Top: descending orbit, Bottom: ascending orbit).

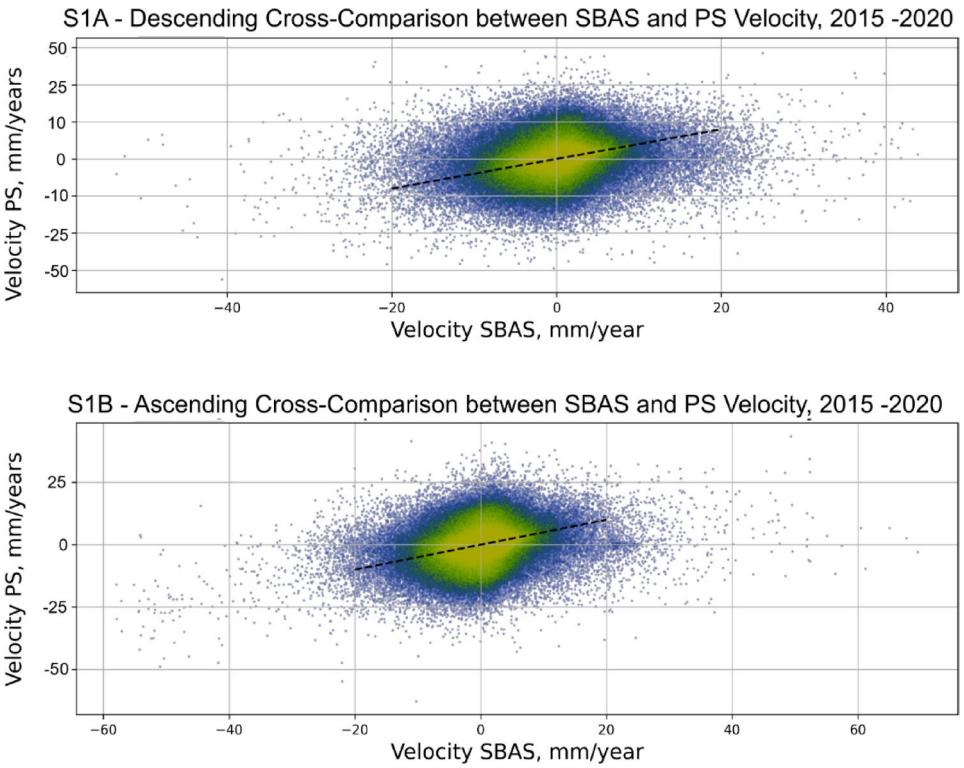


Fig. 15. Comparison of the results between SBAS and PS velocity methods.

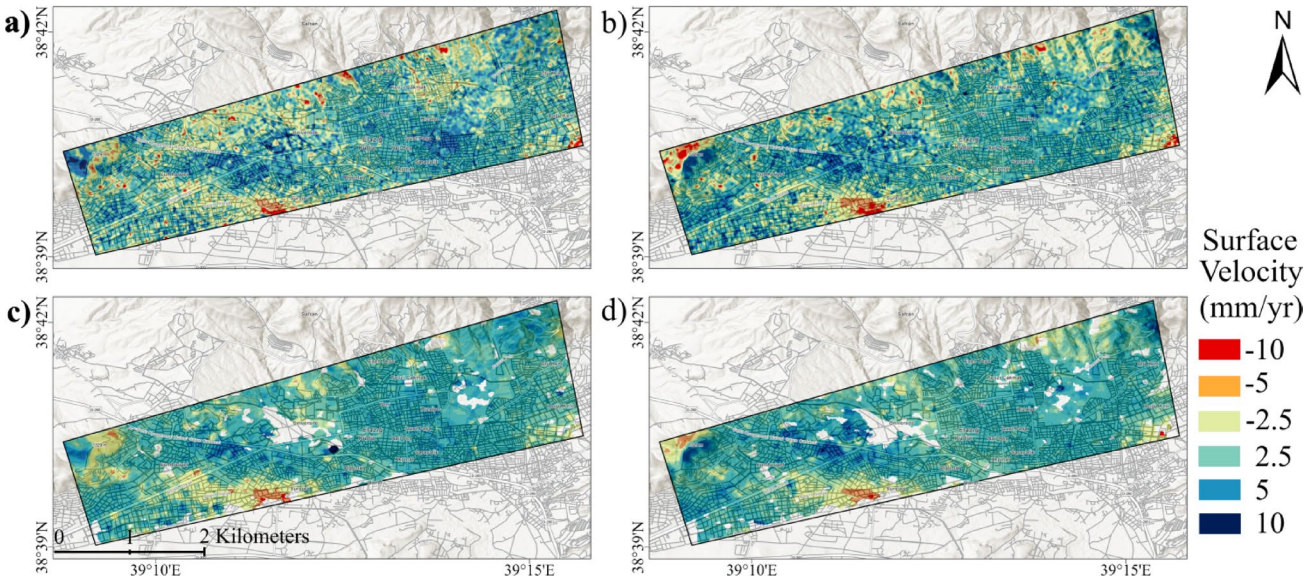


Fig. 16. Annual surface velocity maps obtained from InSAR time-series analysis (**a**: PSInSAR Ascending, **b**: Descending, **c**: SBAS Ascending, **d:** Descending). The maps were generated using ArcGIS Pro[24].

Damage level	Grade 1	Grade 2	Grade 3	Grade 4	Grade 5
Formation (%)					
Alluvium	35	38	34	56	55
Conglomerate, Sandstone, Mudstone	26	26	24	18	17
Ophiolite	5	5	4	2	4
Claystone	4	3	7	1	5
Limestone	12	10	14	11	4
Magmatic Rocks	18	18	17	12	15

Table 5. Geological substrate of the buildings.

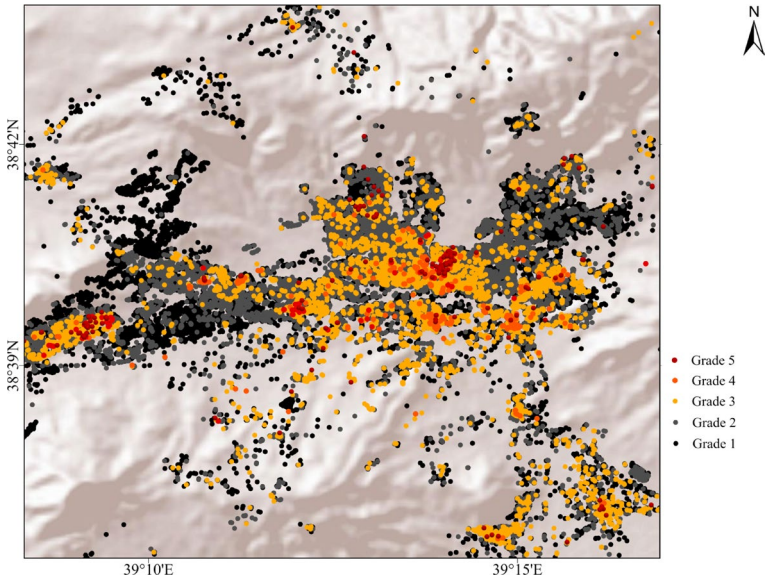


Fig. 17. Map of building damage classes for the Sivrice Earthquake. The map was generated using ArcGIS Pro[24].

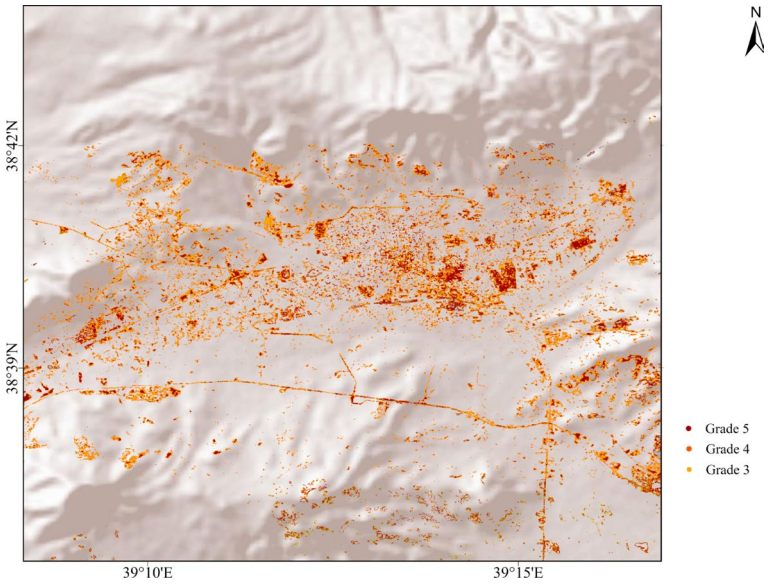


Fig. 18. Optical imagery-based damage map for the Sivrice Earthquake (Grade 5: Collapsed, Grade 4: Severely damaged, Grade 3: Heavy damage, Grade 1 and Grade 2 classes are not included in this map). The map was generated using ArcGIS Pro[24].

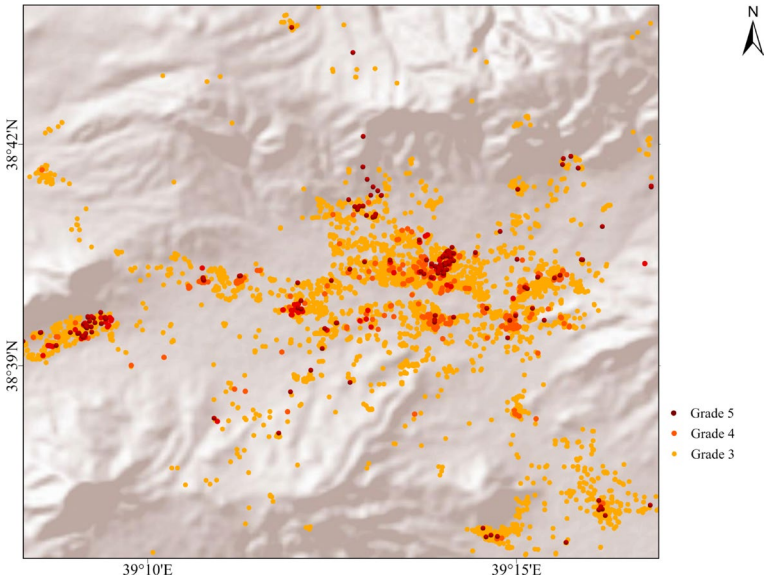


Fig. 19. Sivrice Earthquake damage map (Grade 5: Collapsed, Grade 4: Severely damaged, Grade 3: Heavy damage). The map was generated using ArcGIS Pro[24].

graded, with higher velocities flagged as higher-risk zones. Building structures were classified as either masonry or reinforced concrete, each with distinct vulnerability characteristics. We also factored in additional variables such as the number of storeys, EDC ratings, and distance to active fault lines. By synthesizing these parameters, the analysis revealed how different geotechnical and structural profiles collectively influence the extent of building damage.

The findings derived from RS and GIS techniques were integrated with digitized datasets, facilitating an in-depth analysis of the parameters contributing to structural damage. The variation of the parameters according to the distance from the earthquake epicenter is shown in the combined analysis of the generated displacement maps, pre- and post-earthquake data, and the building inventory (see Supplementary Table S6 online).

The fault distance parameter represents the shortest horizontal distance from each building's coordinate to the nearest mapped fault. The building type refers to the structural system of the buildings, indicating whether they are masonry or reinforced concrete structures, while the number of storeys denotes the total floor count of each building. EDC defines the seismic design requirement level assigned to a site, based on the expected

ground motion intensity and soil characteristics, as outlined in national seismic codes[42]. The surface velocity rate represents the average ground deformation rate over the five years preceding the earthquake, derived using advanced InSAR techniques. Lastly, the geological formation parameter characterizes the underlying lithology at each building location, which plays a significant role in the amplification of seismic waves and thus in potential structural damage.

Besides, EDC was determined according to the Turkish Building Earthquake Code[42] regarding the parameters of map-based short-period spectral acceleration coefficient (SDS) and Vs30 concerning DD-2 design earthquake level which corresponds to the earthquakes with a 10% probability of exceedance in 50 years. Herein, EDC is defined to have values between 1 and 4 for four SDS levels, namely higher than 0.75, 0.50–075, 0.33–0.50, and lower than 0.33, respectively. The influence of variables such as the distance of buildings to the nearest fault, building type, EDC, surface velocity, Vs30, Coulomb stress, and number of storeys on building damage classifications, as well as the inter-variable correlations, was analyzed to assess the seismic vulnerability of buildings and characterize the geospatial and structural attributes of the study area.

In this study, we employed Pearson correlation analysis to measure the linear relationships between these parameters and building damage, offering statistical insights into their direct associations in which values close to 1 and -1 present positive and negative intervariable correlations, respectively (Fig. 20)[43].

Further, SHAP (Shapley Additive exPlanations) analysis was conducted to identify the key factors influencing building damage (Figs. 21, 22). SHAP, a game-theoretic approach, provides a comprehensive understanding of feature contributions by quantifying the impact of each variable on model predictions[44]. This method allows for an interpretable assessment of how different structural and environmental parameters affect damage severity. Figure 21 shows the SHAP values for individual input variables based on their importance score for impacting the building damage. More specifically, the SHAP summary plot given in Fig. 22 for each variable indicates the importance and the trend of each variable regarding the building damage. The order of importance of the input variables is shown in the vertical axis from top to bottom, and the horizontal axis represents the effect of each variable on the model output, namely, the building damage. Accordingly, positive values represent an increase in building damage and vice versa.

By integrating these two approaches, we ensured a robust evaluation of influential factors, combining model interpretability with statistical correlation to enhance damage assessment accuracy. In this manner, the damage

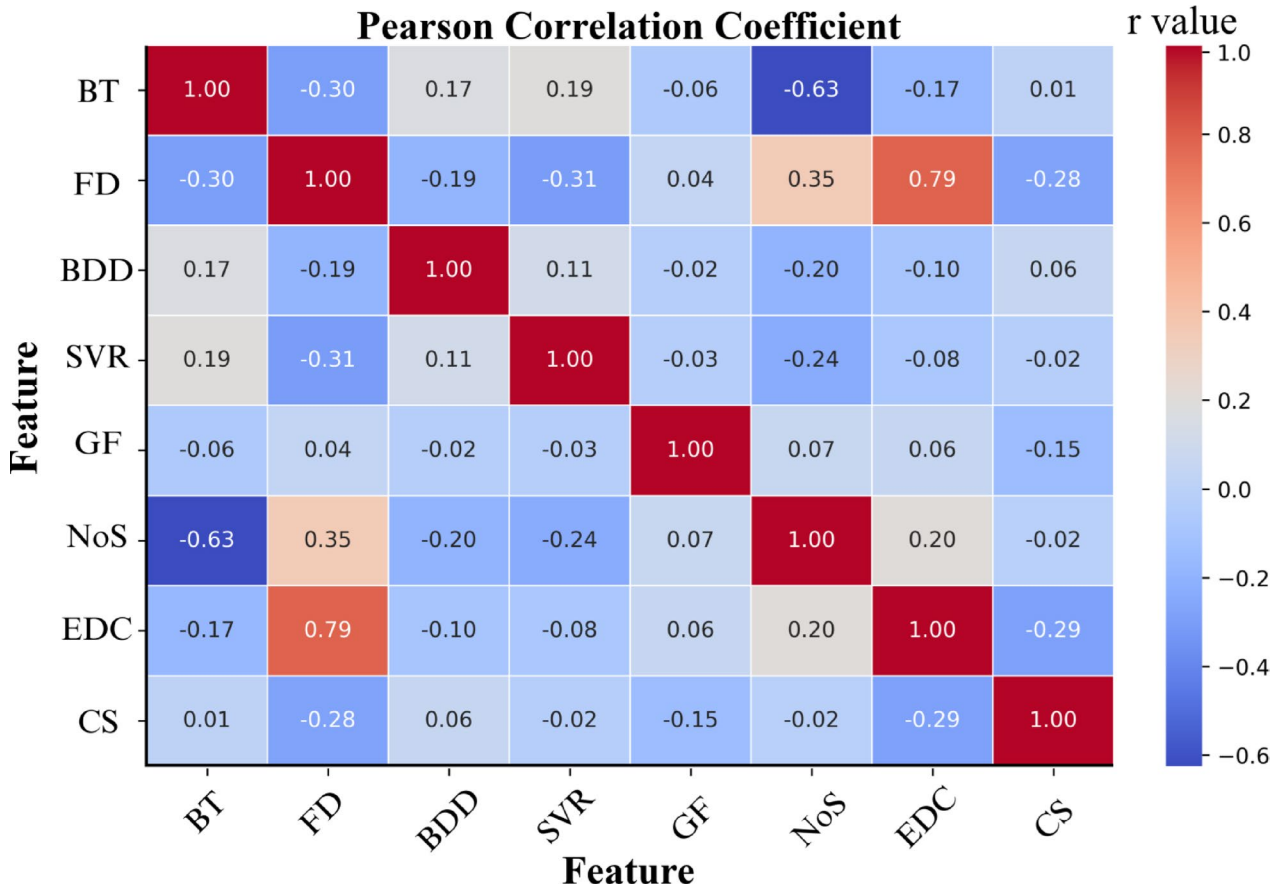


Fig. 20. Pearson correlation coefficient matrix of the analyzed variables (X and Y axes represent the variables: BT: Building type, FD: Fault distance, BDD: Building damage degree, SVR: Surface velocity rate, GF: Ground formation, NoS: Number of storeys, EDC: Earthquake design class, CS: Coulomb stress values). The color scale indicates the strength and direction of the correlation between variable pairs.

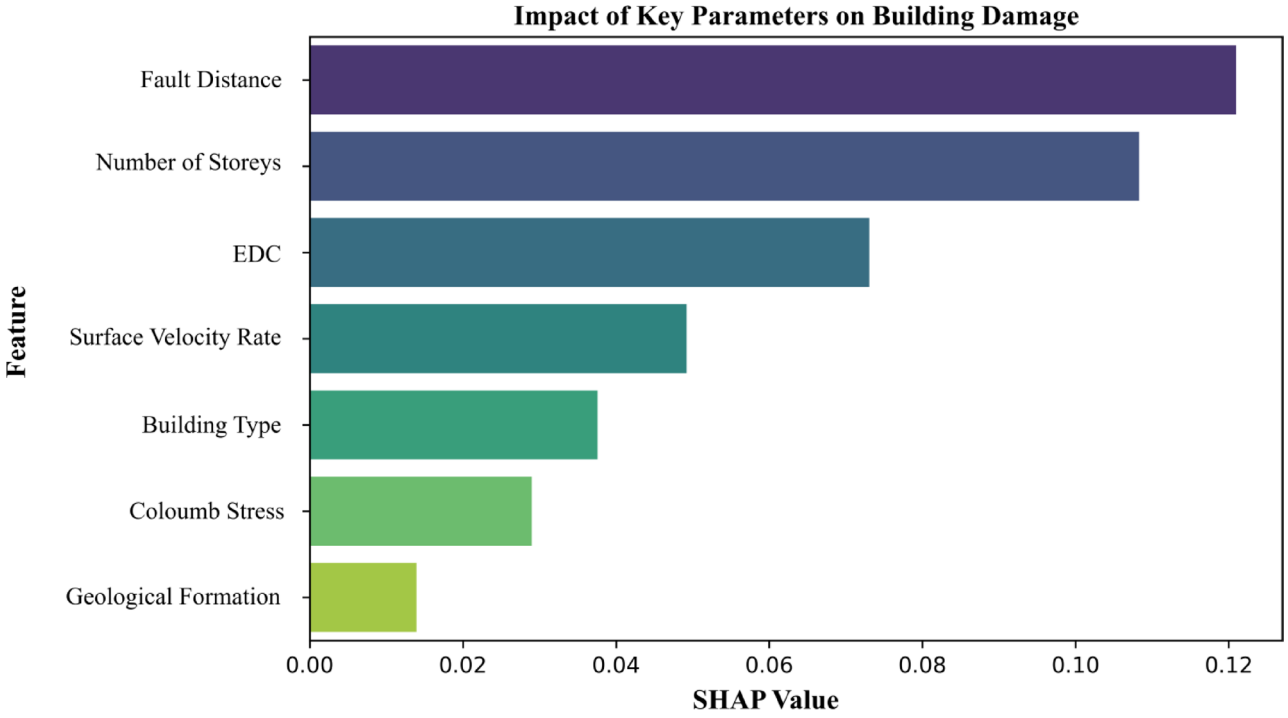


Fig. 21. Importance score of input variable.

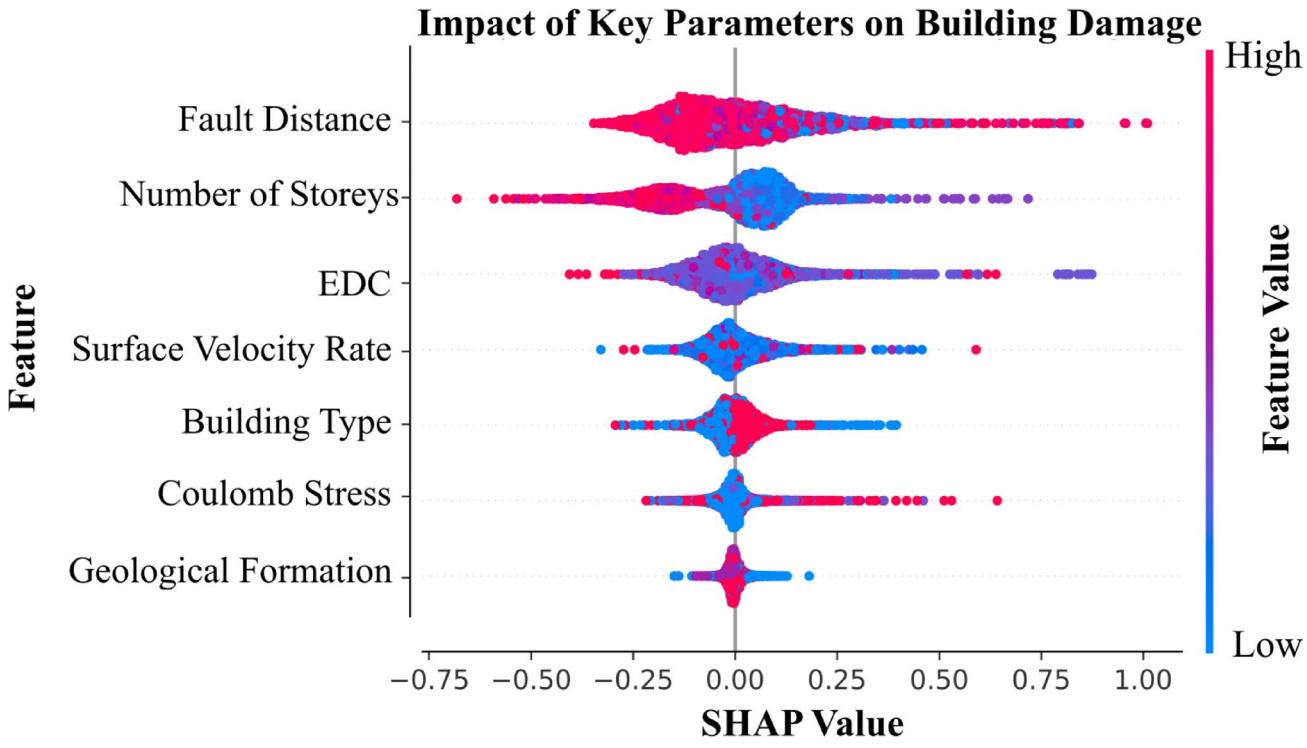


Fig. 22. Impact of key parameters on building damage: a SHAP perspective.

estimation map was generated through the comprehensive integration of RS and GIS methodologies, which included an in-depth analysis of multiple critical parameters to ensure a precise and robust assessment (Fig. 23).

The generated map is founded on the principle that the rise in damage classification level is directly proportional to the values of critical parameters identified through Pearson and Shapley analyses. This mapping approach superimposes high-value parameters to evaluate their cumulative impact on damage classification.

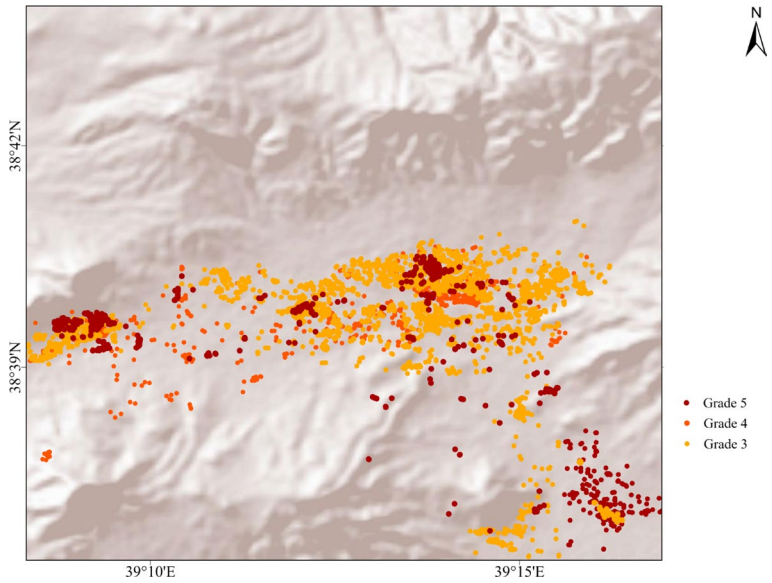


Fig. 23. Damage estimation map for Elazığ city center. The map was generated using ArcGIS Pro[24].

Thus, the extent of structural damage in buildings depends on multiple factors, including fault distance, building type, surface velocity, soil composition, EDC values, number of storeys, and Coulomb stress parameters. Each of these variables plays a crucial role in determining the severity of damage during seismic events.

Regions with elevated Coulomb stress are more prone to failure and may be dynamically triggered by nearby earthquakes. If triggered, this can lead to stronger ground shaking and increased structural damage in the affected area[45]. Similarly, as surface velocity increases, the corresponding ground motion becomes more severe, weakening structural integrity and exacerbating damage levels. Soil composition is another critical factor; higher values indicate reduced ground stability, particularly in areas with alluvial deposits, thereby increasing the likelihood of structural failure. Although high-rise buildings are generally seen as more vulnerable to seismic forces, our analysis shows lower damage in these structures within the study area. This likely results from differences in construction practices and site conditions: low-rise buildings are often older, unreinforced masonry structures built by residents with limited engineering oversight, while high-rise buildings are constructed according to modern engineering standards, using current structural and geotechnical knowledge. Additionally, taller structures are often located on more stable ground with favorable soil properties, which reduces the risk of ground-induced structural failure. The combination of modern construction methods and stable site conditions likely accounts for the observed lower damage in higher-storey buildings.

Moreover, the structural characteristics of buildings significantly impact their resilience. Buildings with higher EDC values exhibit increased vulnerability, leading to higher damage classifications. Similarly, buildings with higher values (indicating masonry structures rather than reinforced concrete ones) are more likely to sustain greater damage, as masonry buildings are generally less resistant to seismic forces than reinforced concrete structures. Conversely, an increase in the number of storeys appears to correlate with lower damage severity, likely because high-rise buildings are generally more recent constructions and are thus subject to modern building codes and seismic regulations. As the proximity to the fault decreases, seismic intensity and ground acceleration peak, leading to higher damage classifications in areas closest to the fault (Figs. 2 and 3)[26].

Discussion

Due to resolution limitations, identifying severely damaged building classes in optical imagery is not feasible. Therefore, this study adopts an alternative approach for detecting such damage using optical images. Immediately after the earthquake, severely damaged buildings still appear within the settlement class. However, by overlaying change detection results from images obtained three months, six months, and one year after the earthquake, the demolition of severely damaged buildings was identified through a time-series analysis of optical imagery.

During the optical analysis phase of the study, it was observed that not all buildings marked for demolition were correctly identified in the land use classification by using LULC maps. This discrepancy arose because some demolished buildings were rebuilt before all urgent demolitions had been finalized. Therefore, images from different periods within the study area were combined, enabling land-use classification for various temporal phases. The change detection areas obtained from these classifications were overlaid with the coordinates of buildings demolished due to the earthquake. This analysis achieved approximately 90% accuracy in detecting the collapsed buildings, and the accuracy was observed to increase with decreasing buffer (Table 2).

Displacements detected using the DInSAR method were analyzed, revealing that ground and building displacements generally decreased with increasing distance from the earthquake epicenter. We observed that buildings classified as Grade 5 (collapsed) had an average surface velocity of 3.9 mm/year, whereas Grade 1 (non-damaged) buildings had an average of 2.5 mm/year, based on PS and SBAS results. This notable increase

of approximately 56% indicates that elevated surface deformation rates may have played an indirect role in the observed structural failures.

The evaluation criteria consisted of the building type and number of storeys obtained from the building inventory, along with additional parameters such as EDC, Vs30, distance to the closest fault (fault distance), surface velocity, and Coulomb stress distribution in the region. The negative correlation between damage classes and fault distance is expected since the buildings in proximity to the epicenter will be subjected to higher accelerations and more severe damage during the earthquake as given in Figs. 2 and 3. The higher damage observed in low-rise buildings is attributable to the fact that approximately half of these buildings are located very close to the earthquake epicenter (see Supplementary Table S6 online).

As shown in Fig. 20, the positive correlation between the fault distance and EDC (0.79) shows the attenuation of earthquake-induced accelerations with the distance of the buildings to the fault rather than a soil-induced amplification. The negative correlations with the Coulomb stress, fault distance (−0.28), and EDC (−0.29) verify the increase in the Coulomb stresses in proximity to the fault while amplifying the accelerations leading to higher EDC values. For the surface velocity rate, the negative correlations with the fault distance (−0.31) verify the expected increase in the surface velocity rate close to the fault. The significant correlations with the remaining parameters are related to the characteristics of the study area namely, (a) the number of storeys and the building type (−0.63), (b) surface velocity rate and number of storeys (−0.24) and (c) shear velocity and fault distance (−0.31) in which the building stock are shown to be major of low-rise masonry or high-rise reinforced concrete buildings, majorly low-rise buildings are located close to the fault and the locations in proximity the fault are of stiff soils with high Vs30 or vice versa, respectively.

Parallel to the Pearson correlation analysis results, it is shown in SHAP analysis results that the variables of fault distance, number of storeys and EDC have the strongest effect among the other input variables of surface velocity, building type, Coulomb stress and geological formation (e.g., Vs30) (Figs. 21, 22). As shown in Fig. 22, the fault distance, the number of storeys and EDC are the most important factors in the prediction of damage classes, while the other variables have less influence. As the epicentral distance of a building decreases, and the number of storeys and EDC increase, the damage class tends to increase.

These factors were collectively considered to assess building damage. The comprehensive analysis of all results indicates that no single parameter solely influences building damage. Instead, multiple factors, including building type and number of storeys, distance to the fault, surface velocity rates, and EDC values, each contribute marginally on their own but collectively have a significant impact. These findings underscore the complex interplay between geological, geophysical, and structural factors in seismic risk assessment and highlight the necessity of integrating these variables into predictive damage models for more accurate and reliable hazard mitigation strategies.

Conclusion

This study demonstrates a multi-source methodology that integrates Sentinel-1 SAR and Sentinel-2 optical imagery with GIS-based damage and ground parameter analyses to assess earthquake-related building damage. By applying supervised classification to Sentinel-2 time-series images (see Supplementary Table S2), we successfully identified both immediate and delayed building collapses. Notably, the method captured not only buildings that collapsed during the earthquake, but also those later demolished by authorities due to severe structural damage.

In the second part of the study, we analyzed the geotechnical and environmental characteristics of buildings with known damage grades by integrating them with pre-earthquake GIS data. The resulting damage classification map aligned closely with field-labeled building damage data, confirming the effectiveness of this parameter-driven approach. Furthermore, we observed a strong relationship between surface velocity and building damage severity.

The combined results of the Pearson correlation and SHAP analysis confirm that fault distance, number of storeys, and EDC are the dominant parameters influencing building damage classification in the study area. Additionally, the negative correlation between building type and number of storeys indicates a structural pattern dominated by either low-rise masonry or high-rise reinforced concrete buildings, with low-rise structures typically located closer to the fault.

These results underline the critical influence of both seismotectonic conditions and structural characteristics on earthquake vulnerability and demonstrate the robustness of the proposed multi-parameter approach in explaining post-seismic damage patterns. These results provide decision-makers and seismic risk planners with a rapid, scalable tool for assessing urban vulnerability without requiring exhaustive field surveys. Integrating surface displacement data and geotechnical variables offers a robust, transferable framework for prioritizing mitigation efforts in high-risk regions.

Future work will apply this approach to the February 6, 2023, Kahramanmaraş earthquakes—also located along the East Anatolian Fault—to evaluate the method's generalizability. By validating this framework across different seismic events, we aim to support urban planning strategies further and reduce vulnerability in future earthquakes.

Data availability

The datasets generated and/or analysed during the current study are not publicly available due to restrictions imposed by the relevant Ministry, which prohibit public dissemination. However, the RS and GIS data used in this study may be made available upon reasonable request, subject to approval by the data provider. Requests for access to these data should be directed to Yusuf Gedik (gediky21@itu.edu.tr).

Received: 21 May 2025; Accepted: 19 September 2025
Published online: 24 October 2025

References

1. Özkan, A. Determination of the kinematics of active faults in the northeastern Mediterranean region by GPS observations and elastic half-space dislocation model (PhD thesis). Graduate Education Institute, Department of Geomatics Engineering. https://polen.itu.edu.tr/bitstreams/232bf3ca-9a77-4585-a3aa-62d82f5f754c/download (2021).
2. Sümer, E. & Turker, M. An integrated earthquake damage detection system. *Int. Arch. Photogramm. Remote Sens. Spatial Inf. Sci.* **36**, 6 (2006).
3. Santemiz, P., Alyuz, N., Cavdar, D. & Alagoz, F. Post-earthquake damage assessment using satellite imagery. https://doi.org/10.1109/ICSPC.2007.4728389 (2007).
4. Arca, D. Afet yönetiminde coğrafi bilgi sistemi ve uzaktan algılama. *Karaelmas Fen ve Mühendislik Dergisi* **2**(2), 53–61 (2012).
5. Wahl, D. E., Jakowatz, C. V. & Yocky, D. A. A new optimal change estimator for SAR coherent change detection. U.S. Department of Energy Report. https://doi.org/10.2172/1159161 (2014).
6. Rao, A., Jung, J., Silva, V., Molinario, G. & Yun, S. H. Earthquake building damage detection based on synthetic-aperture-radar imagery and machine learning. *Nat. Hazard.* **23**(2), 789–807. https://doi.org/10.5194/nhess-23-789-2023 (2023).
7. Minh, D. H. T. et al. Quantifying horizontal and vertical movements in Ho Chi Minh city by Sentinel-1 radar interferometry. Research Gate. https://doi.org/10.20944/preprints202012.0382.v1 (2020).
8. Liu, J., Xinjiang, S. & Yin, J. Y. Automatic recognition of damaged town buildings caused by earthquake using remote sensing information: Taking the 2001 Bhuj, India, earthquake and the 1976 Tangshan, China, earthquake as examples. *Acta Seismol. Sin.* **17**(6), 686–696. https://doi.org/10.1007/s11589-004-0008-2 (2004).
9. Sırmacek, B. & Unsalan, C. Damaged building detection in aerial images using shadow information. In *4th International Conference on Recent Advances in Space Technologies 2009 (RAST '09)*, 249–252 (Istanbul, Turkey, 2009). https://doi.org/10.1109/10.1109/RAST.2009.5158206.
10. Stramondo, S., Bignami, C., Chini, M., Pierdicca, N. & Tertulliani, A. Satellite RADAR and optical remote sensing for earthquake damage detection: Results from different case studies. *Int. J. Remote Sens.* **27**, 4433–4447 (2006).
11. Brunner, D., Lemoine, G. & Bruzzone, L. Earthquake damage assessment of buildings using VHR optical and SAR imagery. *Geosci. Remote Sens.* https://doi.org/10.1109/TGRS.2009.2038274 (2010).
12. Leprince, S., Barbot, S., Ayoub, F. & Avouac, J. P. Automatic and precise orthorectification, coregistration, and subpixel correlation of satellite images, application to ground deformation measurements. *IEEE Trans. Geosci. Remote Sens.* **45**(6), 1529–1558 (2007).
13. Türk, T. Hava fotoğrafı ve optik uydu görüntüleri yardımıyla yatay yer değiştirmelerin belirlenmesi. *Havacılık ve Uzay Teknolojileri Dergisi* **6**(1), 71–79 (2013).
14. Saganeiti, L., Amato, F., Nolè, G., Vona, M. & Murgante, B. Early estimation of ground displacements and building damage after seismic events using SAR and LiDAR data: The case of the Amatrice earthquake in central Italy, on 24th August 2016. *Int. J. Disaster Risk Reduct.* **51**, 101924. https://doi.org/10.1016/j.ijdrr.2020.101924 (2020).
15. Alkan, H., Büyüksaraç, A., Bektaş, Ö. & Işık, E. Coulomb stress change before and after 24.01.2020 Sivrice (Elazığ) earthquake (Mw = 6.8) on the East Anatolian Fault Zone. *Arab. J. Geosci.* **14**, 1–12. https://doi.org/10.1007/s12517-021-09080-1 (2021).
16. Ragon, T., Simons, M., Bletery, Q., Cavalié, O. & Fielding, E. A stochastic view of the 2020 Elazığ Mw 6.8 earthquake (Turkey). *Geophys. Res. Lett.* **48**, e2020GL090704. https://doi.org/10.1029/2020GL090704 (2021).
17. Pousse-Beltran, L. et al. The 2020 Mw 6.8 Elazığ (Turkey) earthquake reveals rupture behavior of the East Anatolian Fault. *Geophys. Res. Lett.* **47**, e2020GL088136. https://doi.org/10.1029/2020GL088136 (2020).
18. Cheloni, D. & Akinci, A. Source modeling and strong ground motion simulations for the January 24, 2020, Mw 6.8 Elazığ earthquake, Turkey. *Geophys. J. Int.* **223**(2), 1054–1068. https://doi.org/10.1093/gji/ggaa3 (2020).
19. Melgar, D. et al. Rupture kinematics of January 24, 2020 Mw 6.7 Doğanyol-Sivrice, Turkey earthquake on the East Anatolian Fault zone imaged by space geodesy. *Geophys. J. Int.* **223**(2), 862–874. https://doi.org/10.1093/gji/ggaa345 (2020).
20. Caglar, N., Vural, I., Kirtel, O., Saribiyik, A. & Sumer, Y. Structural damages observed in buildings after the January 24, 2020 Elazığ-Sivrice earthquake in Türkiye. *Case Stud. Constr. Mater.* **18**, e01886. https://doi.org/10.1016/j.cscm.2023.e01886 (2023).
21. Dedeoğlu, İÖ., Yetkin, M., Calayır, Y. & Erkek, H. January 24, 2020 Sivrice-Elazığ (Türkiye) Earthquake: The seismic assessment of the earthquake territory, geotechnical findings and performance of masonry buildings. *Iran. J. Sci. Technol. Trans. Civ. Eng.* **48**(4), 2393–2412. https://doi.org/10.1007/s40996-023-01318-0 (2024).
22. Hacilar, H., Dedeturk, B. K., Ozmen, M., Eraslan Celik, M. & Gungor, V. C. Accelerated artificial bee colony optimization for cost-sensitive neural networks in multi-class problems. *Expert Syst.* https://doi.org/10.1111/exsy.70045 (2025).
23. General Directorate of Mineral Research and Exploration (MTA). 1:100,000 scale geological map of Elazığ–K42 sheet (JPEG format). Ankara, Turkey: MTA (2023).
24. ArcGIS Pro. ESRI ArcGIS Pro (version 3.1, ESRI, https://www.esri.com) (2023).
25. Boore, D. M., Joyner, W. B. & Fumal, T. E. Equations for estimating horizontal response spectra and peak acceleration from western north American earthquakes: A summary of recent work. *Seismol. Res. Lett.* **68**(1), 128–153. https://doi.org/10.1785/gssrl.68.1.128 (1997).
26. United States Geological Survey (USGS). https://earthquake.usgs.gov/earthquakes/eventpage/us60007ewc/map (2020).
27. Heath, D. C., Wald, D. J., Worden, C. B., Thompson, E. M. & Smoczyk, G. M. A global hybrid VS 30 map with a topographic slope–based default and regional map insets. *Earthq. Spectra* **36**(3), 1570–1584. https://doi.org/10.1177/8755293020911137 (2020).
28. Minister of Environment, Urbanisation and Climate Change - MoEUCC (30 Jan 2024). Retrieved from https://www.csb.gov.tr/hasar-tespit-aciklamalariyla-ilgili-kamu-spotu-yayinda-bakanlik-faaliyetleri-38444 (accessed 11 September 2025).
29. Alaska Satellite Facility (ASF). Sentinel-1 SAR Data. Available at: https://search.asf.alaska.edu
30. Esri, Maxar, Earthstar Geographics, & GIS User Community. World Imagery [Basemap]. In ArcGIS Pro (Version 3.1) [Software]. Retrieved from https://services.arcgisonline.com/ArcGIS/rest/services/World_Imagery/MapServer (2025).
31. European Space Agency (ESA). Sentinel-2 Multispectral Data. Available at: https://dataspace.copernicus.eu
32. Cohen, J. A coefficient of agreement for nominal scales. *Educ. Psychol. Measur.* **20**(1), 37–46. https://doi.org/10.1177/001316446002000104 (1960).
33. Otsu, N. A threshold selection method from gray-level histograms. *IEEE Trans. Syst. Man Cybern.* **9**, 62–66 (1979).
34. Deng, Y. & Wu, C. Analyzing built-up areas in Landsat imagery using an object-based Otsu method. *Int. J. Remote Sens.* **34**, 5730–5748 (2013).
35. Du, Y., Zhang, Y. & Ling, F. Monitoring urban expansion using Landsat imagery and Otsu thresholding. *Remote Sens. Lett.* **7**, 601–610 (2016).
36. Zhang, Q. & Wang, J. A fast algorithm for building extraction in high-resolution images. *IEEE Geosci. Remote Sens. Lett.* **1**, 53–56 (2003).
37. Ferretti, A., Monti-Guarnieri, A., Prati, C., Rocca, F. & Massonnet, D. InSAR Principles: Guidelines for SAR Interferometry Processing and Interpretation (TM-19). (ed. Fletcher, K., Tech. coord. Lichtenegger, J.) ESA Publications, Noordwijk, The Netherlands, ISBN 92-9092-233-8. http://www.esa.int/esapub/tm/tm19/TM-19_ptB.pdf (2007).
38. Ferretti, A., Prati, C. & Rocca, F. Nonlinear subsidence rate estimation using permanent scatterers in differential SAR interferometry. *IEEE Trans. Geosci. Remote Sens.* **38**, 2202–2212. https://doi.org/10.1109/36.868878 (2000).

39. Pechnikov, A. mobigroup/gmtsar: pygmtsar-v2023.3.11 (v2023.3.11). https://doi.org/10.5281/zenodo.7725132 (2023).
40. Sandwell, D., Mellors, R., Tong, X., Wei, M. & Wessel, P. GMTSAR: An InSAR processing system based on generic mapping tools (2011).
41. Konca, A. Ö. et al. From interseismic deformation with near-repeating earthquakes to co-seismic rupture: A unified view of the 2020 Mw6.8 Sivrice (Elazığ) eastern Turkey earthquake. *J Geophys. Res. Solid Earth* **126**, e2021JB021830. https://doi.org/10.1029/2021JB021830 (2021).
42. Disaster and Emergency Management Agency (AFAD), Turkish building earthquake code 2018, TBEC 2018. https://www.resmigazete.gov.tr/eskiler/2018/03/20180318M1-2-1.pdf (2018).
43. Lundberg, S. M. & Lee, S. I. A unified approach to interpreting model predictions. In *Advances in Neural Information Processing Systems*, Vol. 30. https://doi.org/10.48550/arXiv.1705.07874 (2017).
44. Benesty, J., Chen, J., Huang, Y. & Cohen, I. Pearson correlation coefficient. In *Noise Reduction in Speech Processing. Springer Topics in Signal Processing*, Vol. 2 (Springer, Berlin, Heidelberg, 2009). https://doi.org/10.1007/978-3-642-00296-0_5.
45. Stein, R. The role of stress transfer in earthquake occurrence. *Nature* **402**, 605–609. https://doi.org/10.1038/45144 (1999).

Acknowledgements

This work was supported by research grant from the Scientific and Technological Research Council of Türkiye (Project No: 121E406). The authors acknowledge the use of ArcGIS Pro (ESRI, Version 3.1) and Esri World Imagery basemap (used under license, https://www.esri.com) for map creation and visualization. The authors wish to express their gratitude to the Earth3Bee Lab—3D Earth Modeling Laboratory for providing access to their facilities and resources for image processing. The authors would also like to sincerely thank civil engineer Enes Doğan for his valuable insights and constructive contributions throughout the damage assessment phase of this study.

Author contributions

Y.G., O.Ö., and S.S.A. performed the data analysis. M.Ö. provided the data and contributed to the interpretation of the analyses. O.Ö. also played a key role in the selection of analytical methods and the interpretation of the results. All authors reviewed and approved the final manuscript.

Funding

This work was supported by research grant from the Scientific and Technological Research Council of Türkiye (Project No: 121E406).

Declarations

Competing interests

The authors declare no competing interests.

Additional information

Supplementary Information The online version contains supplementary material available at https://doi.org/10.1038/s41598-025-21320-y.

Correspondence and requests for materials should be addressed to M.Ö.

Reprints and permissions information is available at www.nature.com/reprints.

Publisher's note Springer Nature remains neutral with regard to jurisdictional claims in published maps and institutional affiliations.

Open Access This article is licensed under a Creative Commons Attribution-NonCommercial-NoDerivatives 4.0 International License, which permits any non-commercial use, sharing, distribution and reproduction in any medium or format, as long as you give appropriate credit to the original author(s) and the source, provide a link to the Creative Commons licence, and indicate if you modified the licensed material. You do not have permission under this licence to share adapted material derived from this article or parts of it. The images or other third party material in this article are included in the article's Creative Commons licence, unless indicated otherwise in a credit line to the material. If material is not included in the article's Creative Commons licence and your intended use is not permitted by statutory regulation or exceeds the permitted use, you will need to obtain permission directly from the copyright holder. To view a copy of this licence, visit http://creativecommons.org/licenses/by-nc-nd/4.0/.

© The Author(s) 2025